Research Signpost
37/661 (2), Fort P.O.
Trivandrum-695 023
Kerala, India

Remote Sensing Optical Observations of Vegetation Properties, 2010: *** - ***
ISBN: 978-81-308-0421-7; Editors: Fabio Maselli, Massimo Menenti and Pietro Alessandro Brivio

10. Thermal infrared observations of heterogeneous soil-vegetation systems

L.Jia[1] and M.Menenti[2]
[1]*Alterra, Wageningen University and Research Centre, The Netherlands*
[2]*Delft Institute of Earth and Planetary Observation Systems (DEOS), Delft University of Technology Delft, The Netherlands*

Abstract. Heterogeneous soil-foliage systems are characterized under most conditions by large differences in surface temperature between foliage and soil. Two radiometric methods in the thermal infrared spectral region can be used to observe these effects: observations at very high spatial resolution to capture individual leaves or observations at multiple view and illumination angles. The latter is applicable at any spatial resolution, although the anisotropy of emittance is a secondary effect due to thermal heterogeneity and requires high precision radiometric measurements. This chapter reviews the experimental evidence on the anisotropy of emittance by the soil-vegetation system and describes the interpretation of this signal in terms of the thermal heterogeneity and geometry of the canopy space. Observations of the dependence of exitance on view angle by means of ground-based goniometers, airborne and space-borne imaging radiometers are reviewed first to conclude that under most conditions a two-components, i.e. soil and foliage, model of observed Top Of Canopy (TOC) brightness temperature is adequate to interpret observations. Modeling approaches to describe radiative transfer in the soil-vegetation-atmosphere system, with emphasis on

Correspondence/Reprint request: Prof. Dr. Massimo Menenti, D Delft Institute of Earth and Planetary Observation Systems (DEOS), Delft University of Technology, 2629 HS Delft, The Netherlands.. E-mail: m.menenti@tudelft.nl

the thermal infrared region, are reviewed. Given the dependence of observed TOC brightness temperature on leaf-level radiation and heat balance, energy and water transfer in the soil-vegetation-atmosphere system must be included to construct a realistic model of exitance by soil-vegetation systems. Algorithms to estimate foliage and soil temperatures by inverse modeling of multi-angular measurements of exitance are described and evaluated against both synthetic and experimental data.

1. Introduction

1.1. Vegetation – atmosphere exchanges of energy and water

The exchange of energy between the land surface and the atmosphere and within terrestrial vegetation canopies is a significant determinant of processes in the atmospheric boundary layer and in terrestrial ecosystems. In these processes it is crucial to determine accurately the partitioning of available energy into sensible heat flux density (heating or cooling of the surface) and latent heat flux density (evaporation from surface) over a wide range of spatial and temporal scales. Observation and modeling of turbulent heat fluxes at the land surface has been a very active area of research at least since the work of Bowen [1] on the relative magnitude of heat transfer over dry and wet surfaces [2-10]. Most conventional techniques that employ point measurements to estimate the components of energy balance are representative only of local scales and cannot be extended to large areas because of the heterogeneity of the land surface, of the dynamic nature and of the spatial distribution of heat transfer. Remote sensing is one of the few techniques to provide representative measurements, of e.g. surface temperature and albedo, at regional and global scales.

Methods using remote sensing techniques to estimate heat exchange at the land-atmosphere interface fall into two main categories: 1) use surface radiometric temperature to calculate then obtain as the residual of the energy balance equation [11-13]; 2) use to estimate the Crop Water Stress Index or the evaporative fraction (the ratio of evapotranspiration to the available energy) [14-16]. The former category can be further subdivided into single-source, dual-source and multi-source models corresponding with a single-, dual- or multi-layer schematization of the surface respectively. Successful estimations of heat fluxes have been achieved over horizontal homogeneous surfaces, such as a surface fully covered by vegetation, open water and bare soil [17-19]. Large deviations from these conditions occur at partial canopies which are geometrically and thermally heterogeneous. Recent years have seen increasing

evidence of specific difficulties inherent to the heterogeneous nature of terrestrial vegetation. For instance, in many semi-arid environments where the surfaces are partially covered by vegetation, both the soil surface and cooler foliage determine the heat exchanges. This leads to the challenge of relating the separate contributions from these elements to the turbulent transport of heat across the land-atmosphere interface.

Exchange of water and CO_2 between land surface and atmosphere determines to a significant extent the dynamics of the Convective Boundary Layer (CBL) [20-23]. Over homogeneous land surfaces the controlling factor is the partition of net radiation into sensible, latent and soil heat flux. The partition of net radiation is determined by the presence and functioning of vegetation and by available soil moisture. Heterogeneous land surfaces compound the complexity of these processes, since the spatial pattern of land surface properties determines CBL motion at small length scales [22,24].

These studies brought the attention of a wide scientific community to the need for significant improvements in models of such land surface processes and of the interactions of land surfaces with the atmosphere [e.g. 25, 26]. High resolution atmospheric models may be used to interpret observations in complex landscapes as for example done by [27, 28], in the framework of the Hei He basin International Field Experiment (HEIFE).

Observations of the anisotropic emittance of land cover provide unique access to the thermal heterogeneity of soil- vegetation systems. All land surfaces are anisotropic and in the thermal-infrared domain, the directional variation of emitted fluxes (described by the so-called brightness temperature) is mainly determined by the distribution of temperature and emissivity between the elements of the canopy, and by the structure of the vegetation [see 29-31]. Similar to the solar domain, the distribution of shadowed and illuminated parts, as well as the amount of soil and vegetation observable from a particular direction, are the main drivers of the anisotropy models that have been developed to describe the directional variations in thermal infrared spectral domain [e.g. 32-35].

Determination of the soil and foliage component temperature requires inverse modelling of observed emittance, which is a challenge [33, 36-40], given the strength of the signals and the accuracy which can be achieved. On the other hand it provides the only opportunity to overcome a major shortcoming of current parameterizations of heat fluxes at the land – atmosphere interface [37].

Observations of foliage and soil temperature provide also a reliable indicator of crop water stress, either directly as soil-foliage temperature difference or indirectly through modelling of soil evaporation and plant transpiration [39,41].

1.1. Photosynthesis: Light use efficiency of sun-lit and shadowed leaves

Observations of leaf and soil temperature are also quite relevant for understanding and modeling carbon exchange between terrestrial vegetation and the atmosphere.

The rate of photosynthesis depends on many factors, including carbon dioxide concentration in the atmosphere, leaf temperature, or mineral deficiencies (in particular nitrogen) in the soil. The nitrogen content of leaves is strongly related to their chlorophyll content [42].

Foliage temperature. Autotrophic respiration is the process by which some of the chemical energy stored by photosynthesis is used by the plants themselves to grow and develop. This process is critical to the carbon cycle because it results in the rapid release of a large fraction of the carbon initially stored through photosynthesis back to the atmosphere. Autotrophic respiration depends on foliage temperature, growth rates and total biomass, as well as on the biochemical composition of the products formed in the plants [43].

Soil temperature. Heterotrophic respiration is the process by which some of the carbon stored in organic soil components is released. The soil carbon reservoir can be very large compared to the above-ground biomass. Understanding the fluxes of carbon to (senescence, mortality) and from (respiration or mineralization) this soil reservoir becomes a major issue when closing the carbon cycle at the local scale.

Heterotrophic respiration is very dependent on soil temperature, and the availability of water and nutrients, particularly nitrogen. Apart from nitrogen fertilization or deposition, symbiotic fixation of atmospheric nitrogen, and leakage or volatilization, the nitrogen cycle is intimately linked to the carbon cycle within the soil via the biotic activity. Evaluation of heterotrophic respiration is a major challenge in the description and modeling of NEP [44,45].

Due to the strong temperature dependence (Figure 1) of both leaf photosynthesis and soil respiration, observations of foliage and soil temperature are useful to understand and model these processes. As regards field experiments, the use of very high resolution TIR images is a widely used solution to obtain direct measurements of foliage and soil temperature (see Sect. 6.5). As regards observations from space, the only feasible solution is multi-angular observations of Top Of Canopy (TOC) brightness temperature and subsequent inverse modeling to determine foliage and soil temperature from observed anisotropy of emittance. A minimum of two spectral bands is required to establish the brightness temperature of the surface, taking atmospheric influences into account.

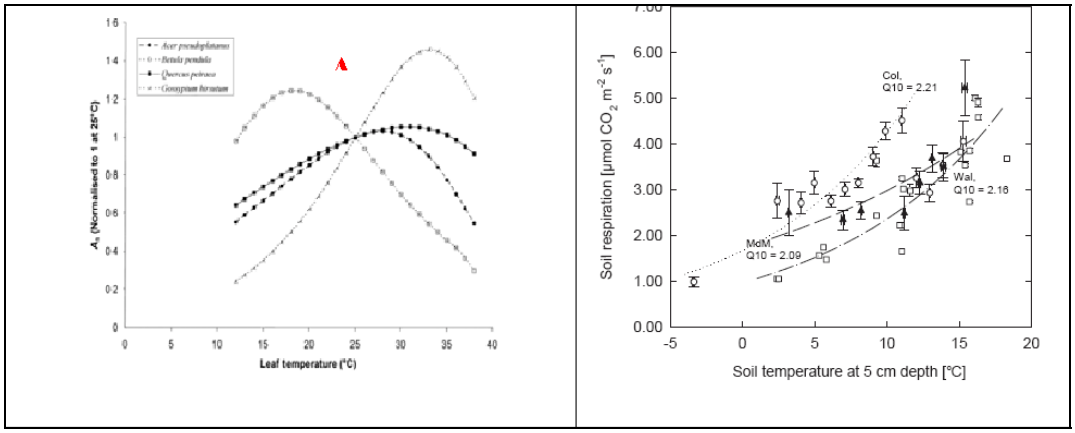

Figure 1. Carbon fluxes and component soil and foliage temperatures: (left) relative net photosynthesis, An (normalized to the observed value at 25°C), vs. foliage temperature [43]; (right) soil respiration vs. soil temperature (after [44]).

2. Nature of anisotropic emittance of land surface

2.1. Anisotropic emissivity of leaves and soils

The observed anisotropy of land emittance is (see Sect. 3) caused by a combination of two different processes: the inherent anisotropic emissivity of terrestrial materials and the thermal heterogeneity of complex, three-dimensional (3D) land targets. The latter is due to the interaction of radiative and convective energy transfer with the 3D structure of land targets. These processes are briefly reviewed in this section.

The accuracy of radiometric measurements of land surface temperature depends significantly on accurate knowledge of land emissivity. A one per cent uncertainty on surface emissivity can cause about 0.6 degree error on land surface in temperature [46]. An angular variation of emissivity has been observed by a number of scientists either in the field or in the laboratory [47,48]. For example, when sea surface wind produces wavelets, an angular variation of surface emissivity is observed [49,50], and an angular variation of the "effective" surface emissivity has also been observed with satellite data [51,52].

Many efforts have been devoted to measure the directional emissivity of soil, leaves and other natural surfaces. Commonly, emissivity of natural surfaces decreases with increased zenith angle of observation. Becker et al. [47] measured in the thermal infrared band the bi-directional reflectivity (BDR) of different types of bare soils including quartz sands, agricultural soil, and well-calibrated powders, a large variability of the BDR for different samples with no apparent systematic behavior apart from the backscattering

peak was observed and the roughness has large impact on the BDR which means that the same material with different grain sizes may exhibit different angular distributions.

As an example, Figure 2 gives the measured angular variation of emissivity for water, sand, clay, slime, and gravel [53].

To describe the anisotropic emissivity of sands and soils, Snyder et al. [54] defined a so-called anisotropy factor, a:

$$a = \frac{\pi f}{1-\varepsilon} \tag{1}$$

where f is the bi-directional reflectance distribution function (BRDF) of the surface, with the same meaning of the bidirectional reflectivity, the emissivity.

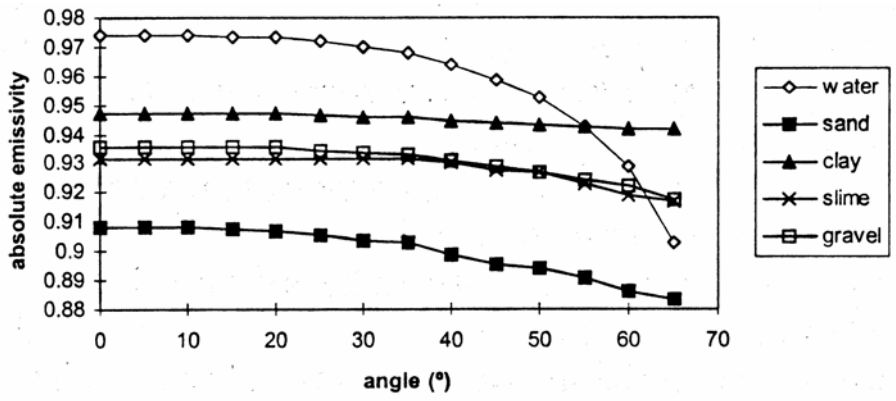

Figure 2. Angular variation of surface emissivity for several natural surfaces (after [53], Fig.3).

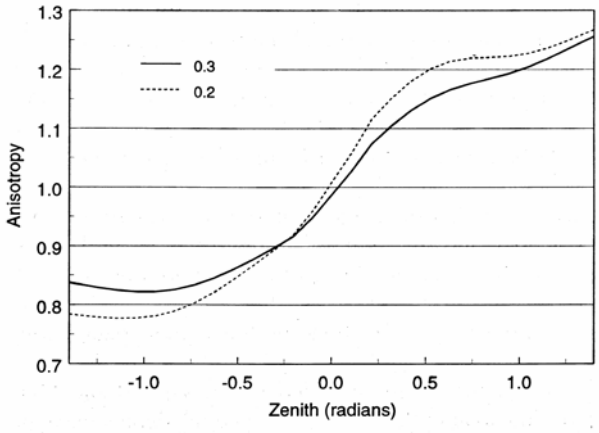

Figure 3. Anisotropy change resulting from changing the single-scattering reflectance from 0.3 to 0.2 in the Hapke model. The plot is in the 30-degree azimuth plane with the angle of incidence at 32 degrees. Positive zenith values represent backscattering (after [54]).

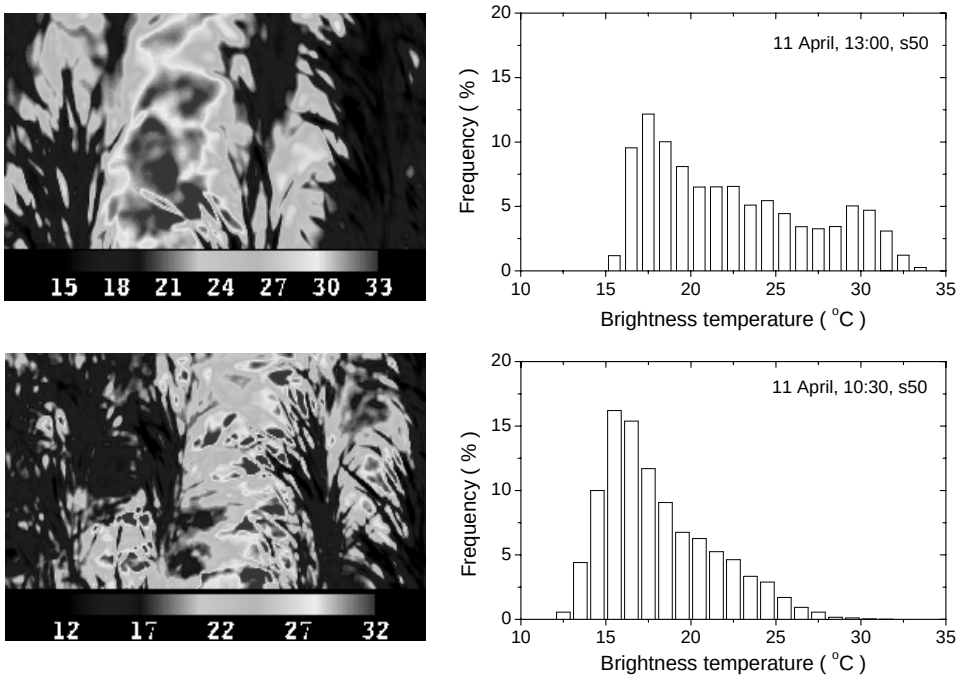

Figure 4. Thermal anisotropy of soil-vegetation system resulting from canopy geometry and variability of absorbed solar radiation by different components: wheat leaves (dark) are significantly colder than soil (light) (after [37]).

To illustrate the magnitude of anisotropy, a simulation with Hapke BRDF model was done by varying single-scattering reflectance and zenith angle (Figure 3). This figure shows that the difference between the two curves for different single-scattering reflectance is relatively small with respect to the overall variation. The simulation by Snyder et al. [54] demonstrates that for typical materials, over a realistic range of azimuth and incident and reflected zenith angles, the upper bounds of the impact of this difference is 4.8% (RMS) and 9.5% (maximum error) respectively.

Efforts to evaluate the anisotropy of foliage emissivity have been limited, because it is very close to unity and has small angular variation. Therefore, for most studies, leaves are assumed to be Lambertian. The ray-tracing method has been applied to estimate the directional reflectance of canopy in VIS/NIR. An extension of this method to the TIR region may be useful to simulate the angular variation of canopy thermal infrared reflectance.

2.2. The 3D structure of vegetation canopies

The architecture of most vegetation canopies leads to a complex three-dimensional distribution of absorbed radiant energy and, therefore, of the local

balance of energy within the canopy space (Figure 4). On the one hand, within the canopy space the surface temperature of foliage and soil varies significantly. On the other hand, the vertical distribution of foliage temperature is also variable with the solar elevation, the density of leaves and the angle distribution of leaves. The thermal heterogeneity within a vegetation canopy leads to the fact that T_{rad} measured by thermal infrared (TIR) sensors is a function of canopy geometry, vertical distribution of foliage temperature T_f, soil temperature Ts, sensor view angle (θ_v,φ_v) and incoming radiation [55,35] (Figure 5).

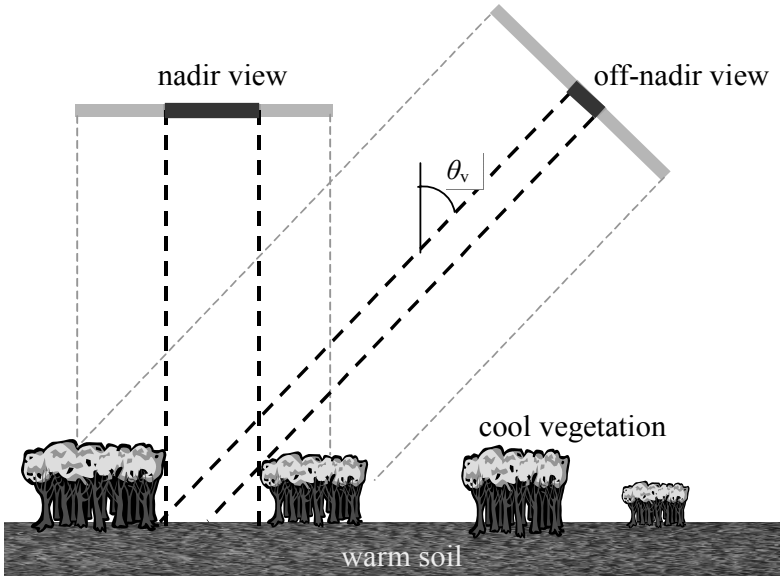

Figure 5. Illustration of observed TIR radiance as a function of canopy geometry, foliage and soil component temperatures and the zenith view angle θ_v. The light gray bar indicates the fraction of foliage in the instantaneous field of view (IFOV) of the sensor, the black bar indicates the fraction of soil in the IFOV [37].

Radiation and convection in the canopy space

For incomplete canopies, a frequent case in nature, the interaction between the canopy and the atmosphere becomes complex due to the canopy geometry in terms of the size and spacing between plants, the leaf density and the leaf angle distribution. Figure 6 illustrates how the elements of a sparse canopy are interacting with their environment. The complex canopy geometry determines the distribution of absorbed solar radiation in the canopy, thereafter inducing spatial variability of sources and sinks of heat and water vapor in the canopy space. A large spacing between plants or lower leaf density, for instance, makes the exposed soil to play an important role in the land-atmosphere interaction. Canopy

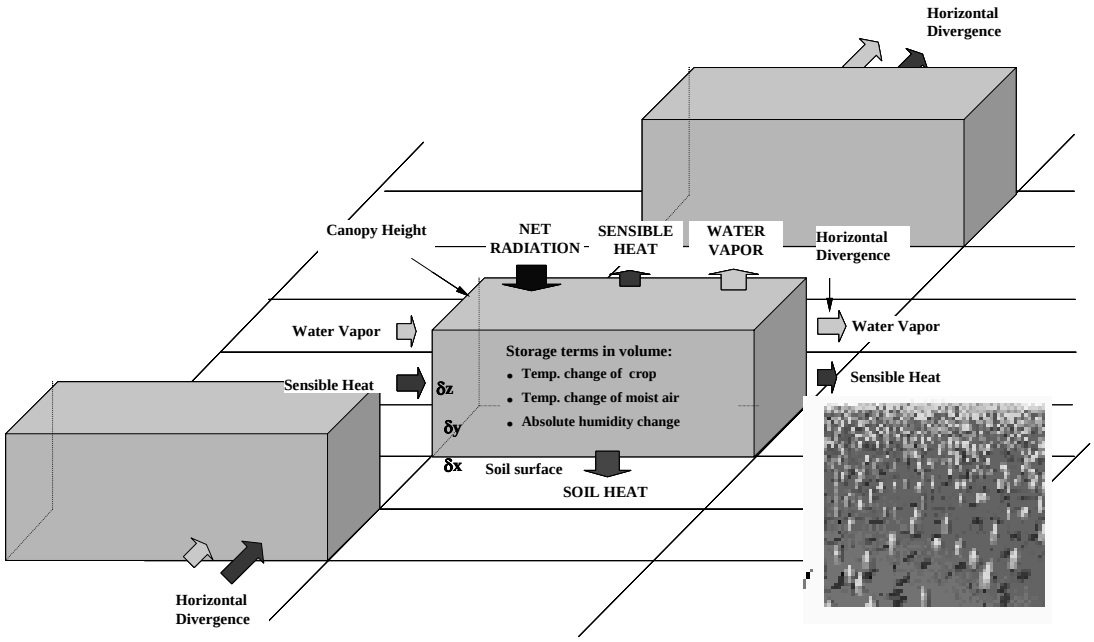

Figure 6. Schematic illustration of the 3D structure of a vegetation canopy and of the interactions between canopy elements and the canopy environment

geometry has also influence on the airflow in the canopy space and the boundary layer resistance of leaves and soil, thus changing the source/sink strength. The interaction between thermodynamic and dynamic processes will lead to thermal heterogeneity, which will in turn give rise to the anisotropy in the exitance of canopy (See e,g, [56,57]).

Thermal heterogeneity of vegetation canopies

The radiative and thermal state of elements in a soil-vegetation canopy system is strongly dependent on its geometric structure (radiative transfer) and on its environmental situation (convection and conduction processes). The interactions between the land surface and the atmosphere consist of the interactions between foliage and soil surface, foliage and air in the canopy space, soil surface and air in the canopy space, and between the soil surface and deeper soil layers, i.e. root zone. A realistic model requires describing the processes involved at each spatial point. However, it may not be possible or necessary to do so. Adequate simplification is necessary to redefine the canopy, which should retain the dominant aspects of 3D radiative, heat and mass transfer (see Sect. 3).

Commonly, the soil temperature is much higher than foliage temperature because of the different thermal properties between soil and foliage. Thus, to simulate energy exchange between canopy and natural environment, vegetative

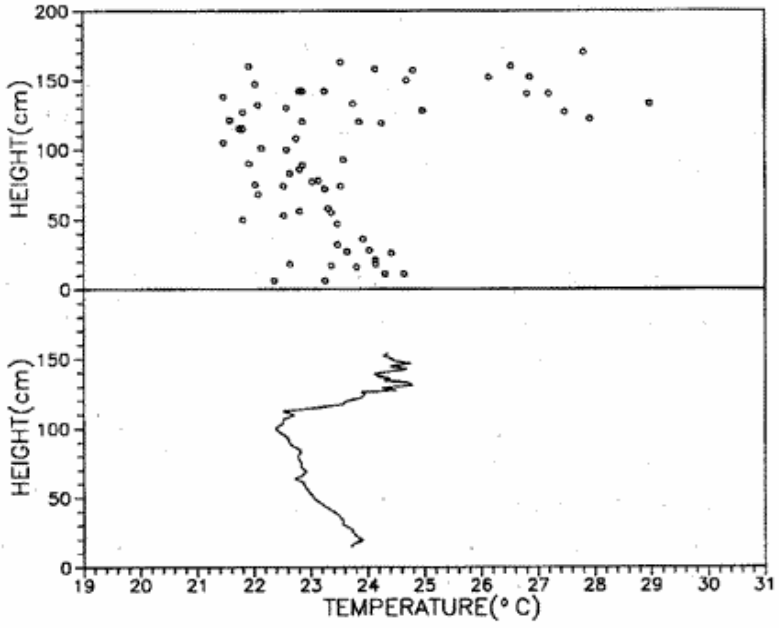

Figure 7. Leaf temperature profile in the canopy, at 1200-1300h, for all days. The top graph shows each individual leaf temperature measurement. The bottom figure shows a 10-point moving average of leaf temperature (after [58], Fig.7).

canopy is commonly represented by two-source model: the sensible heat flux between soil and air, and the one between foliage and air. As the penetration of downwelling solar short-wave radiation and long-wave sky radiation, the foliage temperature changes with the depth of canopy. The temperature profile of vegetative canopy with the height of canopy has been observed by several scientists, e.g. by [58] who measured the variation of leaf temperature with height within the canopy space by means of a Teletemp Infrared Thermometers (Figure 7).

The temperature profile of canopy layers results from the energy balance for each layer. As seen from Figure 7 both foliage at top layers and at bottom layer have higher temperature. The higher temperature of top layer is due to the relatively large incident short-wave radiation which may decrease with depth within the canopy. The bottom layer of vegetative canopy will receive more long-wave radiation than the middle canopy layer from the soil which temperature is usually higher than foliage, with convective cooling being less efficient than at the top of the canopy.

Lei [59] made a detailed temperature measurements of sunlit and shaded leaves of Blackbrush and sunlit soil from March through December 2001 at the Clark Mountain (roughly 35.7°N and 115.5 °W; elevation 1.475 m). Figure 8 shows the temperature difference between sunlit and shaded foliage and the temperature difference between sunlit soil and foliage.

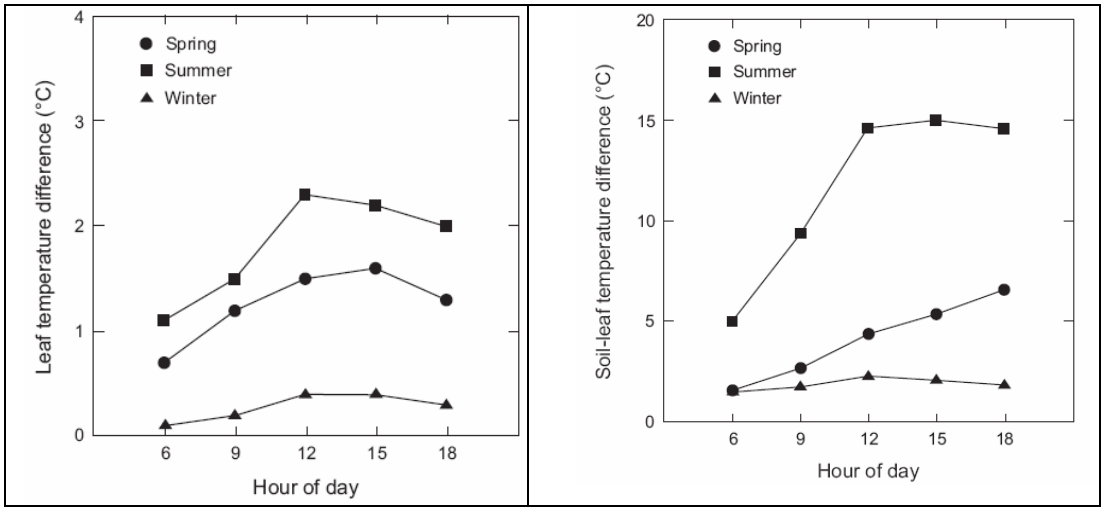

Figure 8. Temperature difference between: sunlit and shaded leaves (left); sunlit soil surface and sunlit leaves(right); Clark Mountain of southeastern California (after [59], Fig.4 and Fig.5)

3. Observed magnitude of anisotropy

3.1. Ground observations of $T_b(\theta)$ at TOC

The anisotropy in canopy exitance implies that *brightness temperature* (T_{b0}) at the *Top Of the Canopy (TOC*) changes with view zenith angle θ_v and azimuth angle φ_v as shown by field measurements over a range of canopies, especially over sparse canopies. The dependence of observed Top Of Canopy (TOC) brightness temperature $T_{b0}(\theta_v,\varphi_v)$ on the view angle is best documented by ground measurements with a goniometer-mounted radiometer (Figure 9, after [37]). $T_{b0}(\theta_v,\varphi_v)$ is the temperature measured by a radiometer at zenith angle θ_v and azimuth angle φ_v and is simply derived from the radiance R_λ measured by a radiometer by inverting the Planck's function. Therefore, the observation of $T_{b0}(\theta_v,\varphi_v)$ and the observation of TIR radiance are equivalent.

In this chapter, for simplification the symbol 'R' denotes only TIR radiance and the subscript TIR will be neglected. TIR radiance of a target is usually referred to as 'exitance', i.e. the sum of emitted and reflected TIR radiance by the target concerned. Nielsen et al., [60] have shown that it is common to have large (up to 20K or more) differences between sun-lit soil and shadowed leaf surfaces, particularly when the top soil is dry. Jackson and Idso, [61] found differences between bare soil and air temperature as large as 27°C. For a soybean canopy with 35% ground cover, the soil temperature exceeded the canopy temperature by 11°C and was 15°C higher than air temperature [55].

Usually, $T_{b0}(\theta_v, \varphi_v)$ is measured by a radiometer in a specific spectral range (centered at some wavelength) and in a particular direction (θ_v, φ_v), within an instantaneous field-of-view (IFOV) Ω_{IFOV}. The portions of canopy components with different surface temperatures in the IFOV will change with the view angle (Figure 9). As a consequence, strong anisotropy in exitance, i.e. a significant variation in $T_{b0}(\theta_v, \varphi_v)$ with the direction of observation, can be observed over thermally heterogeneous systems like sparse canopies. For instance, Kimes and Kirchner [30] observed in a cotton field that the difference in $T_{b0}(\theta_v, \varphi_v)$ between the 0° (mixture of vegetation and soil) and the 80° (vegetation only) zenith view angles was 16.2°C at noon, while the difference was only 0.9°C in the early morning. Lagouarde et al. [62] observed a difference of up to 3.5 K for a corn canopy and 1.5 K for grass (20 cm high) with a view zenith angle between 0° and 60° around solar noon.

A goniometer (Figure 10a) was designed specifically for canopy directional $T_{b0}(\theta_v, \varphi_v)$ measurements [63,37,64]. Two arms are connected perpendicularly to each other with the longer one being fixed onto a circular track, which is set up on the ground, and the shorter one is kept horizontal on

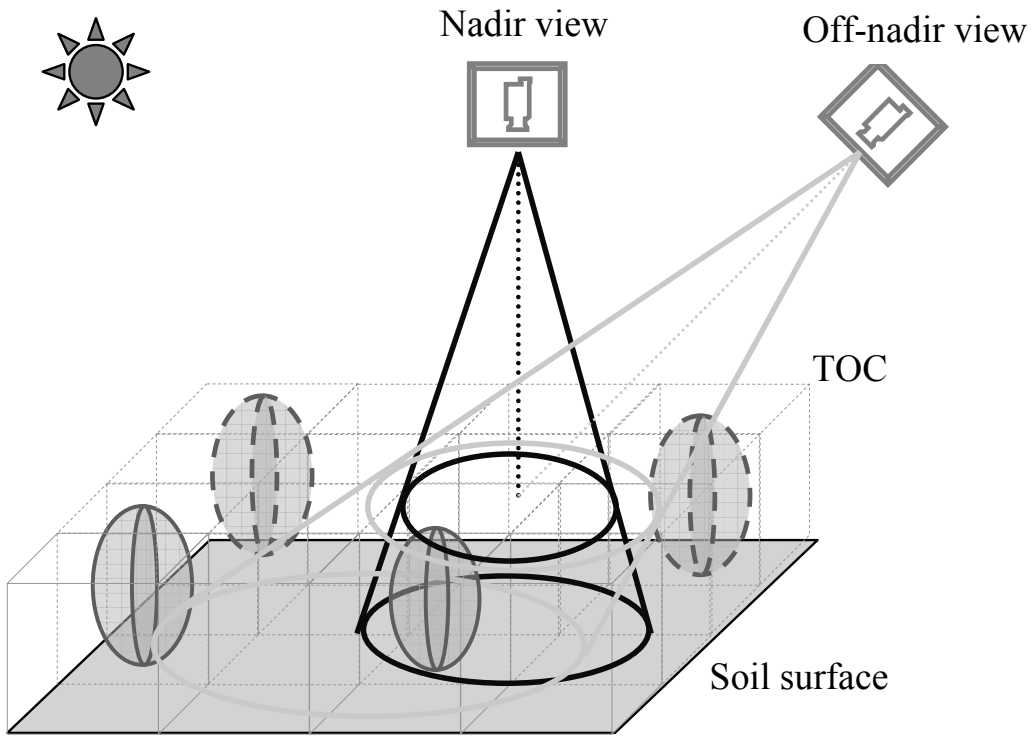

Figure 9. Observation of TOC brightness temperature T_{b0} at different view angles. The circles represent the footprints of IFOV at the Top Of Canopy (TOC) and at the bottom of the canopy for different view angles. The components in the volume between TOC and the bottom are observed by a radiometer located above the canopy [37].

top of which radiometers can be mounted. The longer arm can move along the track to change the azimuth position. At each specific azimuth position φ_v the longer arm sways over a range of zenith angles θ_v (maximum 60º). Such movements are designed and performed to measure the TIR radiance of the same target on the ground (Figure 10b) within a desired range of azimuth and zenith angles. The diameter of the footprint, however, increases with increasing θ_v because of slant viewing. A 10º interval is normally used for the zenith angle change, and 15º interval for azimuth angle change (Figure 10c).

Two radiometers were used [37] to measure $T_{b0}(\theta_v, \varphi_v)$. One radiometer was set up on the top of the short horizontal arm to measure the radiance of the canopy at each azimuth and zenith angle. Distance to the target was the same at any position of the arm so that the radiometer footprint included the same target at all positions as shown in Figure 10b. The other radiometer was mounted on a mast observing continuously the canopy at nadir. The second radiometer provided the continuous measurements needed to correct for the temporal change in the measurements of $T_{b0}(\theta_v, \varphi_v)$ during a complete goniometer scan. The latter usually took about 20 minutes during which the surface temperature may change significantly due to the variation of the solar radiation and windspeed. Due to technical problems, different radiometers were used during the experiment (Table 1).

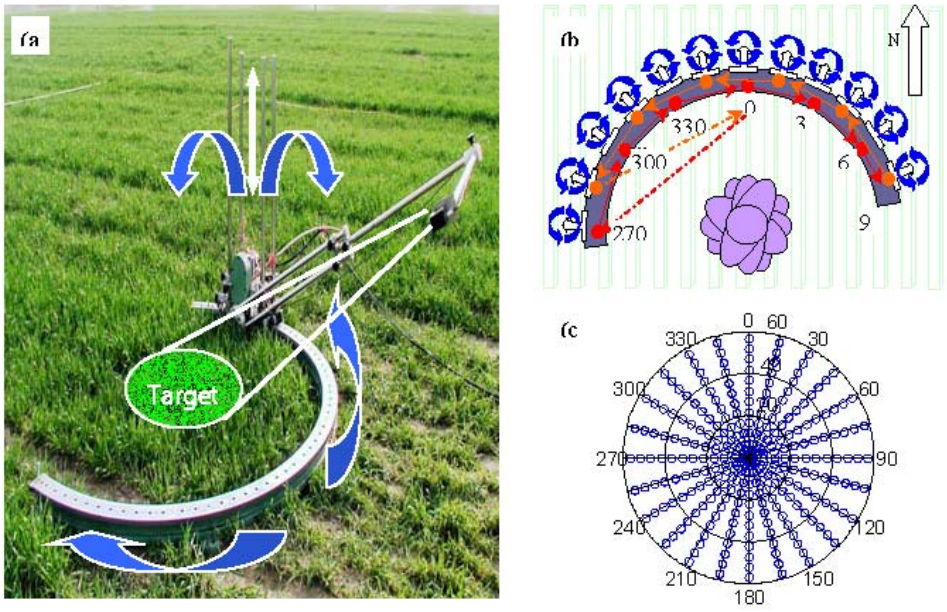

Figure 10. Goniometric system used to measure $T_{b0}(\theta_v, \varphi_v)$: a) overview of the goniometer system and of the footprint of the TIR radiometer; b) zenithal and azimuth sampling scheme; c) detail of the azimuth sampling scheme [37,39].

Table 1. The characteristics of the radiometers used to measure $T_{b0}(\theta_v, \varphi_v)$ during the field campaign of QRSLSP [37].

Instrument	Wavelength (μm)	FOV (º)
Radiometer 1	8 - 11, 10.4 - 14	4.7
Radiometer 2	8 - 11, 10.4 – 14	8.6
Radiometer 3	8 - 11, 10.4 – 14	8.6
Radiometer (single channel)	8 – 14	15
Raytek radiometer	8 – 14	7

A thermal camera (AGEMA THV 900 LW), mounted on top of another goniometer, was used to obtain images of surface temperature of the wheat crop $T_{b0}(\theta_v, \varphi_v)$ for prescribed azimuth and zenith directions. The AGEMA thermal camera has a scanning HgCdTe detector and a Stirling cooler with the single channel covering the spectral range between 8-12 μm, the frame rate is 15Hz for 136x272 pixels, and the nominal sensitivity is 80 mK at 30 °C. The camera was equipped with a lens having a FOV of 5x10°.

Figure 11 shows the change in T_{b0} from nadir to off-nadir view zenith angles at each view azimuth angle at different hours during the two selected days: (a) 11 April and (b) 21 April. Only the measurements across two perpendicular planes are shown: one in the N – S direction along the canopy rows and one in the E – W direction across the row. At each azimuth direction, measurements were made twice, e.g. at both 0° and 90° azimuth the first observation started from θ_v = +60 º through nadir to θ_v = -60 º (denoted as 'go' in Figure 11) and the second observation went back from view zenith θ_v = -60 º through nadir to θ_v = + 60º (denoted as 'back' in Figure 9). All the measurements shown in Figure 11 have been corrected for temporal change taking into account the measurements provided by the second nadir looking radiometer.

Changes in T_{b0} with θ_v are significant and show different trends at different hours during a day. Around noon, the observed near-nadir T_{b0} is always higher than that at off-nadir positions. On the contrary, in the early morning and the late afternoon, near-nadir T_{b0} tends to be lower than the off-nadir values. Maximum difference between near-nadir T_{b0} and those at off-nadir is about 2.8 ºC on 11 April, while 4.4ºC is observed on 21 April, both around noon time.

The row structure of the winter wheat also plays an important role in determining the angular change of T_{b0} . Such structure effects are evident when comparing the shape of the curves in the along-row direction (the plane from 0° to 180°) and the curves in the across-row direction (the plane from 90° to 270°) in Figure 11. The latter shows a steeper slope, particularly in the position

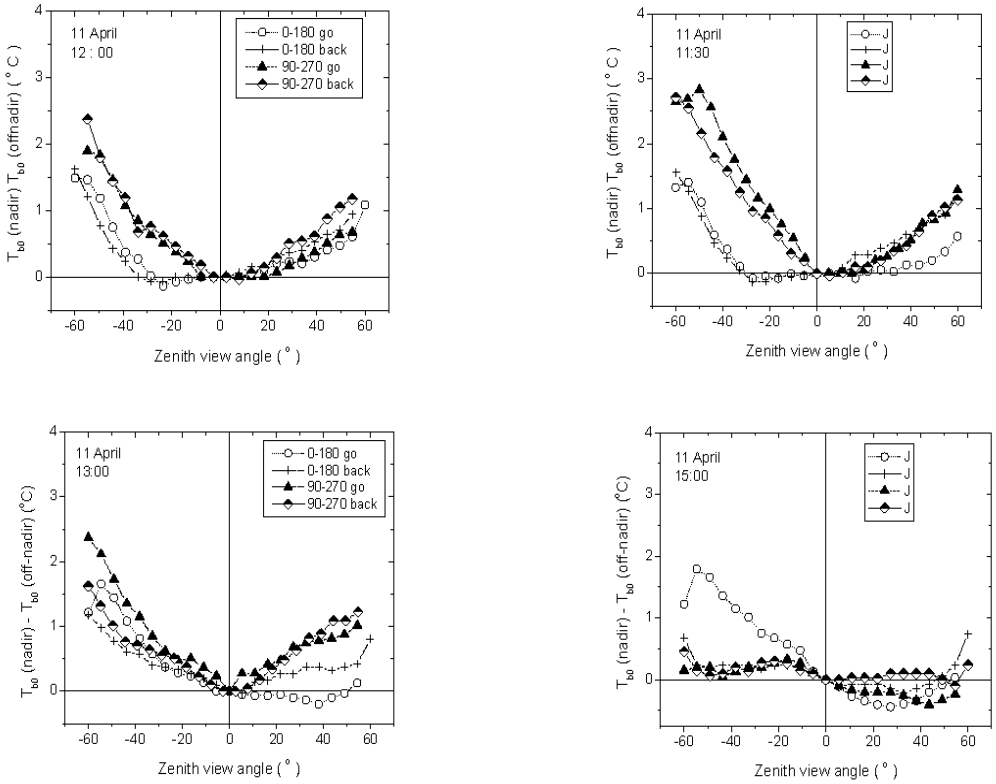

Figure 11. Measurements of the directional variation of TOC brightness temperature difference T_{b0} (*nadir*) - T_{b0} (*off-nadir*) with zenith view angle on 11 April at different times of the day at the QRSLSP site [65]. T_{b0} (*nadir*) is T_{b0} at $\theta_v = 0º$, T_{b0} (*off-nadir*) is T_{b0} measured at $\theta_v \neq 0º$. The positive zenith view angle correspond to the azimuth 0° and 90° planes, the negative zenith view angle correspond to the 180° and 270° azimuth planes [37].

opposite to the sun, e.g. at 270° plane (negative zenith view angle) at 10:30, 11:00 and 11:30 on 11 April 2001 when the sun was located between 90° and 180° planes, and asymmetric than the former.

For the proper interpretation of multi-angular measurements the geometry of observations needs to be taken into account, because of significant differences in footprint size, position and shape at different view angles. The change in the diameter of the radiometer footprint when the radiometer observes the target at different zenith view angles implies significant differences in the canopy elements captured by observations.

3.2. Airborne observations

To our knowledge the only airborne imaging system having the capability to perform multi-angular thermal infrared observations is the Airborne Multi-

angle TIR/VNIR Imaging System (AMTIS) developed by [66]. This is a prototype three-channel multi-angle imaging system. It provides high-resolution data in visible/near infrared and thermal infrared spectral bands for use in deriving bi-directional reflectance factors. The precision of the viewing angle is determined by the pointing precision of the AMTIS and the knowledge of the attitude of the airplane (pitch, roll and heading angles).

The AMTIS consists of one visible CCD camera, one near-infrared CCD camera, one thermal video system (TVS), camera bench, swing assembly, motor driver and controller, exposing synchronization signal generator, data grabber, real-time display and recorder. Two CCD cameras and the TVS are mounted on the camera bench. A stepper motor rotates the camera bench.

The instantaneous field of view (IFOV) of each pixel has been fixed at 0.3 mrad for the VNIR bands, 1 mrad for the TIR band. The total field of view of each camera is about 20°. The altitude range is roughly from 500 m to 10,000 m, which thus translates into a spatial resolution ranging from 0.15 m to 3 m for VNIR, 0.5 m to 10 m for TIR. Normally, AMTIS is operated at an altitude of 3000 m with a ground speed of 250 km/hr, and swing along-track through discrete 9 programmable viewing angles within a range of ±45°. A step motor through a gearbox drives the cameras bench. The accuracy of the pitch angle is 0.3°. The maximum swing speed is 200 steps per second, or 60° per second. Normally, the swing angular velocity is about 10° per second when AMTIS takes photograph, then swings back at the angular velocity of about 30° per second.

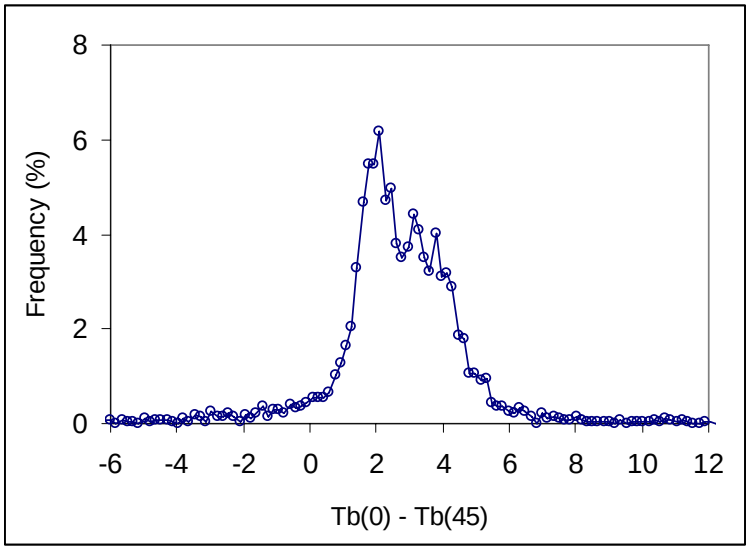

Figure 12. Difference of surface brightness temperature Tb between nadir view and forward view (45 degrees); observations by AMTIS in Shunyi of Beijing on 11 April 2001.

3.3. Space observations of $T_b(\theta)$ at TOA and TOC

The measurements of thermal emission at top of atmosphere include the contributions of atmosphere (through atmospheric upwelling radiation and scattering of surface thermal emission) and those of the surface.

To perform nearly simultaneous observations of $T_{b0}(\theta_v, \varphi_v)$ from space at multiple view angles two technical solutions may be used: a) multiple optics or b) accurate along-track pointing. The Along Track Scanning Radiometer 1 (ATSR-1) flown on ERS-1 was based on solution (a). ATSR-1 was followed by ATSR-2 in 1995 and the Advanced ATSR (AATSR) on ENVISAT in 2001. The characteristics of these systems are summarized in Table 2 and Figure 13.

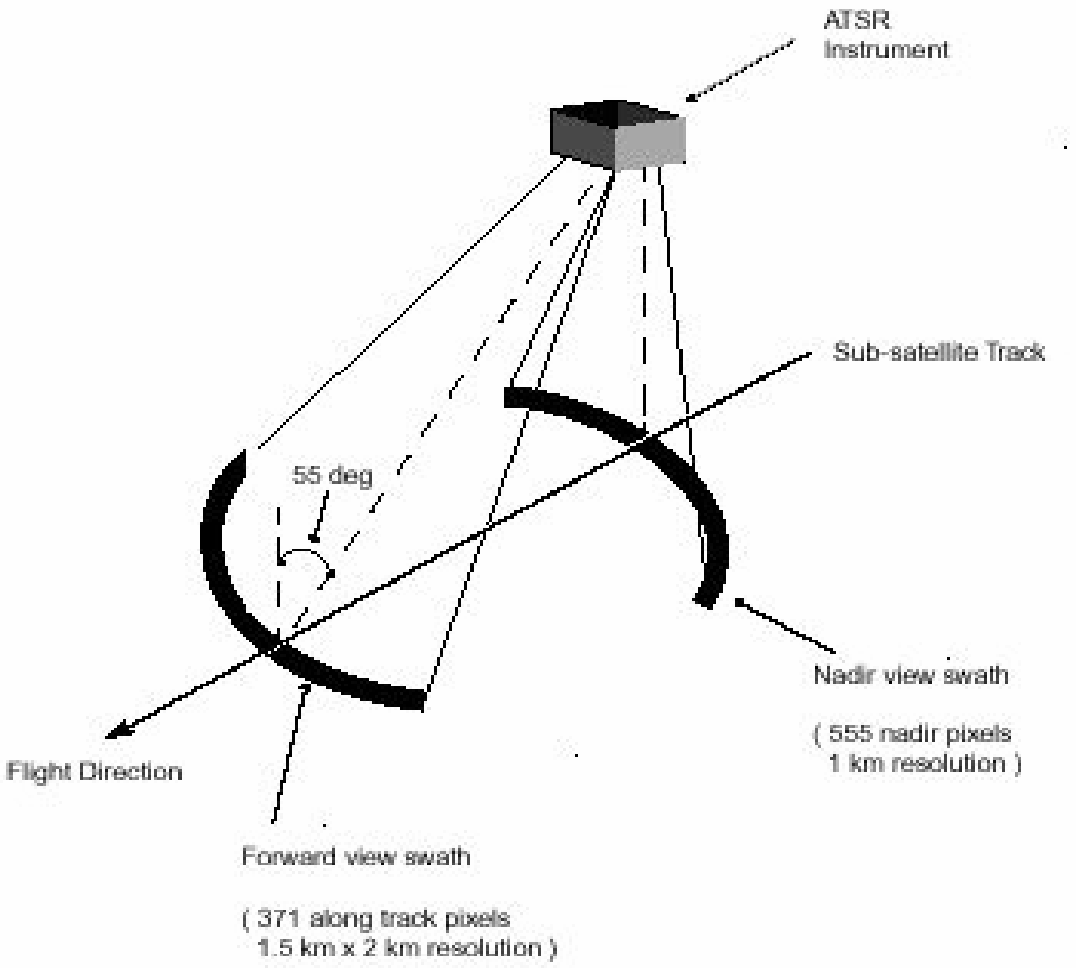

Figure 13. Illustration of Along Track Scanning Radiometer (ATSR) observation (after [67]).

Table 2 Central wavelength and bandwidth of (A)ATSR spectral channels. Symbol '*' indicates ATSR-1 channels.

Channel No.	Central wavelength (μm)	Full width at half maximum (μm)
1	12.0*	11.60-12.50
2	11.0*	10.52-11.33
3	3.7*	3.47-3.90
4	1.6*	1.575-1.642
5	0.87	0.853-0.875
6	0.65	0.647-0.669
7	0.55	0.543-0.565

All ATSR sensors acquire dual-view angle data (approximately 0° and 53° at surface) in four channels for ATSR-1 and seven channels for ATSR-2 and AATSR. The nominal noise equivalent temperature difference (NEδT) of ATSR-2 for IRT channels is 0.04 K. The use of the along track scanning technique (Figure 13) makes it possible to observe the same point on the earth's surface at two view angles through two different atmospheric path within a short period of time. The first view is at a view angle of 55° (approximately 53° at the earth surface) along the direction of the orbit track when the satellite is flying toward the target point, which is referred to as forward observation in this Chapter. Within 2 and half minutes the nadir (0°) view observation is made over the same point, which will be referred to as nadir observation later on. The swath width of ATSR-2 is 500km, which provides 555 pixels across the nadir (0° zenith angle) swath and 371 pixels across the forward (55° zenith angle) swath. The nominal pixel size of ATSR-2 is $1\,\text{km} \times 1\,\text{km}$ at the centre of the nadir swath and $1.5\ \text{km} \times 2\ \text{km}$ at the centre of the forward swath.

The (A)ATSR instruments are imaging radiometers which are currently the only observing system able to provide from space quasi-simultaneous bi-angular radiance measurements of the earth's surface in the TIR and SWIR spectrum regions (in addition to VIS/NIR channels). ATSR-1 onboard the first European Remote Sensing satellite (ERS-1) was launched in July 1991 and operated until June 1996. ATSR-1 had four channels indicated as 'star' symbol in Table 2. ATSR-1 was designed particularly for providing data over the sea. ATSR-2 onboard the ERS-2 satellite was launched in April 1995 and is currently providing data both over land and over sea. In addition to one SWIR channel and three TIR channels as on ATSR-1, ATSR-2 and AATSR have three narrow-band visible-near infrared channels in the blue, green and red spectrum respectively for vegetation monitoring. Table 2 gives information on channel spectral characteristics. (see the World Wide Web site at www.atsr.rl.ac.uk/software.html for details).

The ATSR-2 data analysed below pertain to images acquired on June 6th 1999 over Spain at 10h30am local solar time. The major part of this image is over a cultivated zone, the rest being bare soils. This image is considered cloud-free, inasmuch as ATSR-2 data do not indicate the presence of clouds.

The four images have been corrected for atmospheric effects: channel 1 (12µm) nadir and forward views; channel 2 (11µm) nadir and forward views. Since ATSR has a limited dynamical range of brightness temperatures, and radiometric saturation is supposed to occur at 312 °K, all pixels having $T_b \geq 312$ °K have been masked. Atmospheric corrections have been performed using the split-window method given by Equation 7 [68].

The difference in brightness temperature at a given wavelength and a given view angle between the TOC and TOA levels (Figure 14) indicates the magnitude and the dependence on view angle of atmospheric effects. The temperature at TOC is always higher than the temperature at the TOA level and this difference is larger at the 45° view angle because of the larger atmospheric optical depth. For a given view angle, the difference is larger for channel 1 (12µm) than for channel 2 (11µm) due to the stronger atmospheric absorption in channel 1. The surface anisotropy signature is observable after atmospheric correction (Figure 15). Most pixels show a lower temperature in

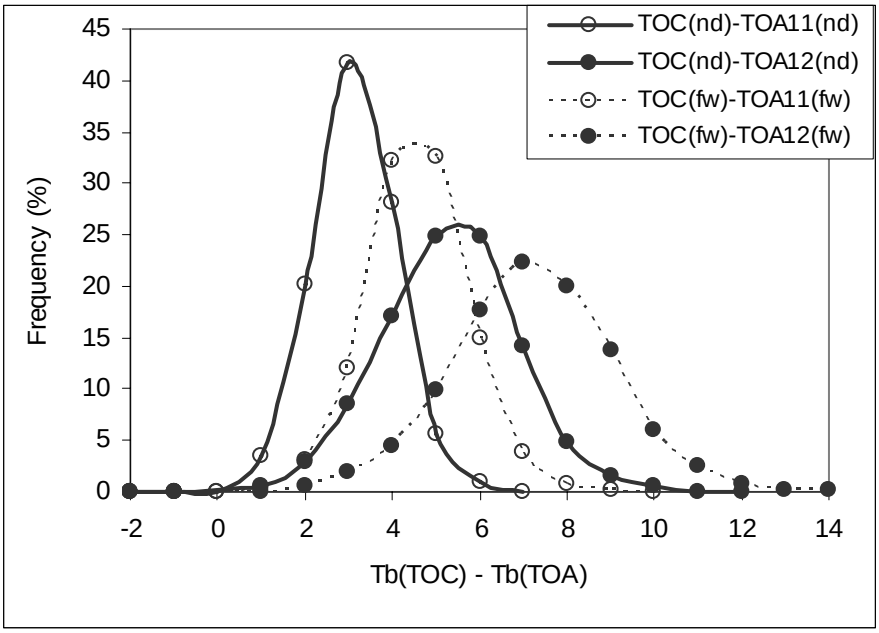

Figure 14. Atmospheric impact on surface brightness temperature for two TIR channels at both nadir and forward views. Data are from ATSR-2 on June 6th 1999 over Spain. (nd=nadir; fw=forward).

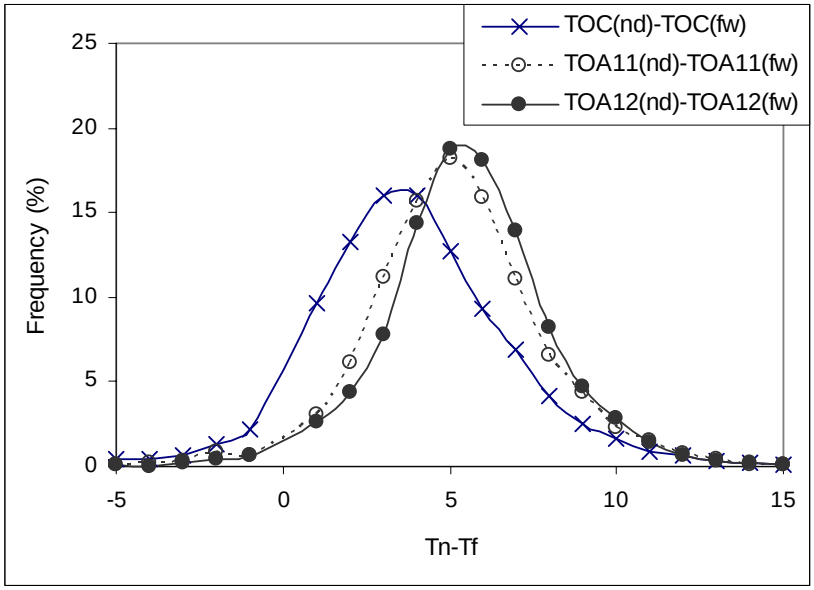

Figure 15. Difference in surface brightness temperature between nadir and forward view at TOC and TOA. Data are from ATSR-2 on June 6th 1999 over Spain.

the forward image than in the nadir image. The histogram peaks around 3.5K at TOC level and around 5.0K and 5.2K at TOA level for channels 2 and 1, respectively. This figure shows also that the angular variation observed at TOA comes from both the angular variation at TOC and the angular dependency of the atmospheric effects, and the effects of atmosphere generally increases the TOA anisotropy signature as compared to the angular variation observed at TOC.

The experimental evidence reviewed in this section leads to conclude that the thermal heterogeneity of soil – vegetation systems is very significant (see e.g. Figures 4, 8 and 11). On the other hand, the same observations suggest that soil– foliage temperature differences are much larger than the difference between sunlit and shadow elements, both foliage and soil. In other words, available data suggest that a 2-components conceptual model of soil – canopy systems may be adequate in most cases, with 4 components (sunlit, shadow; foliage, soil) necessary under extreme radiative forcing. This conclusion leads to the modelling approach presented below.

4. Modeling the anisotropic exitance of soil-canopy systems

4.1 Overview

Several models have been proposed and developed to describe and handle the anistropic exitance of soil – canopy systems. They can be loosely classified in three categories:

Simple geometric (deterministic) model of the system: this approach applies to structured vegetation (row crops, tree lines, patches) inasmuch geometry is known and the system can be described with a small number of known parameters (e.g.: dimensions, soil emissivity, vegetation emissivity, ..). [69-73]. Attempts to incorporate a coupling with the atmospheric radiation (down welling) have been scarce [74]. Such an approach is quite useful for sensitivity studies or to assess the feasibility of the retrieval coupled to the atmospheric correction requirements. Except when the geometry is accurately known, or can be well inferred from other measurements (also from satellite), usefulness of this type of model is however limited since it cannot deal with the physical processes within the system, and model inversion is very sensitive to uncertainties in parameters.

Radiative transfer within the canopy: this approach applies to dense (or less dense) systems that can be described statistically and using biome characteristics. Models in this domain solve radiative transfer in the canopy with atmosphere and soil as boundary conditions, assuming plant type, distribution, plant architecture, LAI (total, horizontally / vertically projected), LIDF, etc. [32, 33, 34,75-80, 29]. Soil temperature, leaf temperature, temperature gradient within the canopy may either be assumed, or simultaneously solved for.

Observed TIR anisotropy may reveal whether there exists a temperature gradient within the canopy or not. However, interpretation of directional radiance implies that all parameters of the system are known or can be accurately retrieved from other measurements (from satellite in the visible, NIR and SWIR domains).

Since the fluxes within the canopy are coupled to the flux above the canopy, the micrometeorological parameters have to be known. It turns out that the surface TIR directional effect is quite sensitive to ambient conditions. Thus, for a given biome, the TIR emitted radiance may reverse the sign of its angular variation with zenith angle (i.e. decrease or increase with increasing zenith angle), or even show no variation at all.

This category of models may not be best for inverse modeling of observations. Nevertheless, such models are extremely useful for: i) for evaluating the order of magnitude of the angular effect that can be expected and ii) for comparing what is observed with outputs of models. It is worth noting that the modeled anisotropy is in no case large, no more than a few K only if large (> 60°), zenith angle can be used.

The Geometric-Optical method was initially proposed to model the radiative transfer through conifer canopy in near infrared and visible domains [81]. After taking into account the component emittances at the pixel scale, the geometric-optics method has been extended to the thermal infrared domain to

model the angular variation of thermal emission from vegetative canopies at the local scale [82]. The core idea behind geometric-optical method is that, a vegetation canopy is assumed to be represented by different component elements with different shapes (such as cone, elliptical, or sphere), the parameters for these shapes (such as height, radius, and apex angle) are specified, the spatial distribution for these canopies in pixel plane is previously determined (random, regular, or row), and the position of solar and sensor is used as input. After accounting for the mutual shading between canopies, the fractions of four components (sunlit foliage, sunlit soil, shaded foliage and shaded soil) are computed through geometrical optical rules. Then the contributions of each component to the reflected or emitted radiance are combined to compute the reflected or emitted radiation at top of canopy level or pixel level. Multi-scattering between different components is also included.

Some improvements on the original geometric-optical method have been implemented to take into account the spatial heterogeneity including clumping index of vegetative canopy which describe the non-random distribution of canopy elements including leaves, branches, and the non-random spatial distribution of vegetative canopies in pixel scale [83].

A limitation of the geometric-optical method is that the mutual shading, gap distribution inside vegetative canopy, multi-reflection, and scattering cannot be accounted for. To overcome this shortcoming, a so-called hybrid geometric-optical radiative transfer method was proposed to improve the original geometric-optical method. By using this geometric-optical radiative transfer method, [84] simulated the directional brightness temperature over a maize canopy with a row structure. The gap probability between rows was computed with geometric-optical rules, while the gap inside rows was calculated with radiative transfer theory. Row and canopy structure parameters including row width, canopy height and width between rows are needed to initialize their model. The comparison between the simulations with their model and in situ measurements showed that, the angular variation of brightness temperature can be precisely captured with this type of model.

Radiosity [85-86] is a computational algorithm to describe the scattering of light between ideally diffuse (Lambertian) surfaces. Although this method has been devoted to modeling bi-directional reflectance distribution function (BRDF) in VIS/NIR optical remote sensing for a long time [87], there are few reports on its application to thermal infrared.

Inhomogeneous thick vegetation layer that can be statistically described by an angle dependent “gap fraction” or “gap frequency” [88]. This approach represents an intermediate situation between 1- and 2-. It allows the directional TIR radiance to be described as a linear combination of the foliage and soil radiance contributions, weighted by the gap fraction. Inverting directional TIR

radiance may be used to retrieve vegetation temperature and soil temperature, assuming, for instance, an angle dependent canopy emissivity. A detailed and comprehensive discussion of direct and inverse modeling is found in [35].

The advantage of this type of models is that the gap fraction can be phenomenologically correlated with measurements in the visible-NIR domain through appropriate vegetation indices [89]. Hence, combination of measurements in the solar reflected domain and in the thermal infrared domain may be of great value, if not yet enough, to solve the problem (i.e.: retrieve soil and foliage temperatures).

A further step can be made by exploiting detailed BRDF (including hot spot as much as possible) measurements from satellites in the visible – NIR domain to assess e.g. LIDF type, that would help improving the gap fraction estimate.

4.2. Detailed 3D models of radiative transfer in vegetation canopies

Realistic simulation of the canopy structure and remote sensing scenario has been developed to model the radiative transfer of downwelling solar radiance and atmospheric radiance reflected by vegetative canopy and soil [90] and of thermal emission from leaves and soil by [91]. The so-called DART (Discrete Anisotropic Radiative Transfer) model has been developed [91-93] to simulate pixel scene and radiation energy budget in this scene. The whole scene is specified by the locations of different objects (including tree, lake, soil, lake, and building) and combined by a 3-D matrix of parallelepiped cells of various sizes. The “atmosphere” part is simulated with “air” cells, while the “terrestrial” part is made up of “air” cells. Cells are associated with 4 types of elements (soil, vegetation, wall, water), with or without relief (DEM, Digital Elevation Model). More details of this model can be found in [91,92].

A realistic representation (Figure 16) of canopy geometry and of the spatial heterogeneity of radiative and convective processes can be constructed using a discrete 3D grid [94]. The grid points are the basic unit in the 3D model dealing with the radiation, heat and water vapor fluxes calculations. The components of radiative environment, such as the direct beam radiation from the sun, the diffuse radiation from the sky and soil, and the diffuse radiation scattered by foliage at any grid point are calculated. This description of geometry may also be used to model convection of heat and water vapor. One should note that since we have assumed wind speed, air temperature and vapor pressure are homogeneously distributed along the horizontal directions, the grid points at the same vertical level have identical values of these variables wherever they are located in the horizontal directions

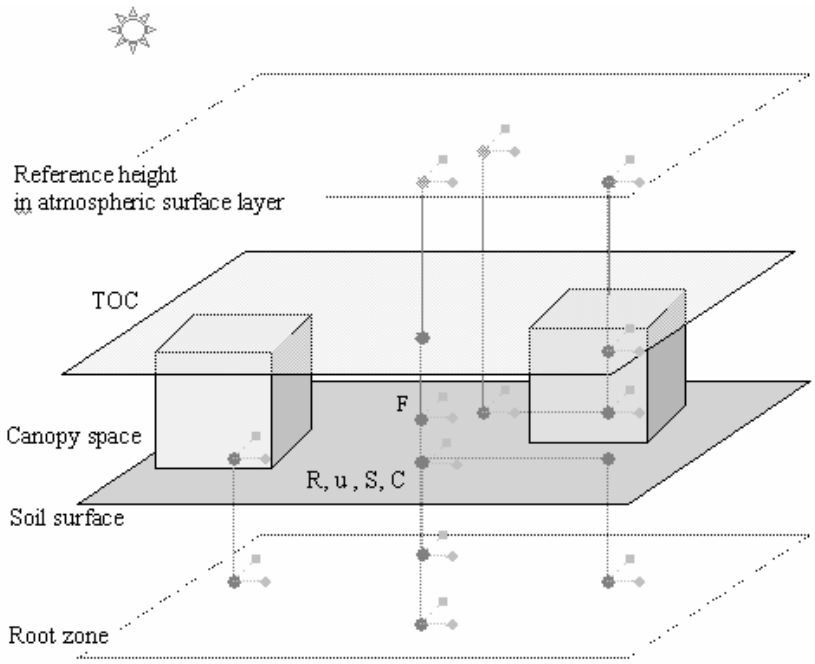

Figure 16. Simplified schematic illustration of interactions between points (either containing foliage or soil) in a three-dimensional canopy (soil + vegetation) and in the atmosphere just above the TOC, with all possible physical, chemical and biophysical processes included. TOC is represented by 'green plane' while soil surface is represented by 'orange plane'. The green blocks represent sub-canopies. Points are symbolized by symbol '●', interaction between points are represented by 'lines'. The symbol implies that the interactions are 3D (vertical and horizontal exchanges). Each point is characterized by absorbed radiation flux density R, windspeed u, concentration C of a scalar (i.e. temperature, moisture, CO_2, etc), source/sink S of a scalar. F represents the flux density of a scalar between points [37].

4.3. Simpler models: Linear vs. non-linear, 2 vs. 4 components mixture models

Typically, the pixel or IFOV (Instantaneous Field Of View) of an imaging radiometer includes both foliage and soil where soil is commonly much warmer than foliage. The experimental evidence reviewed in Sect. 3 suggests that the thermal heterogeneity of a soil-canopy system may be represented under most environmental conditions using foliage and soil components only. Under extreme radiative forcing the difference between sunlit and shaded canopy elements becomes larger. Simple linear and non-linear models have been proposed to simulate radiance or brightness temperature measured at TOC.

A 2-component mixture model can be used to simulate the directional distribution of thermal radiation as [75,76]:

$$B_\lambda(T_{b0}) = f\varepsilon_v B_\lambda(T_v) + (1-f)\varepsilon_g B_\lambda(T_g) \tag{2}$$

where, T_{b0} is the brightness temperature at TOC. ε_v and ε_g are emissivities of foliage and soil, respectively. f is the fractional coverage of vegetation. T_v and T_g are temperatures of foliage and soil, respectively. B_λ denotes the Planck function. Previous study showed that the directional thermal radiation is not sensitive to the uncertainty of soil and leaf emissivities [35]. This model implies that both the multiple reflection between vegetation and soil, and the temperature differences between sunlit and shaded canopy elements are neglected.

It should be noted that equation (2) is a linear representation of directional thermal radiation at top of canopy without taking into account the atmospheric downwelling radiation and the temperature differences between sunlit and shaded elements inside canopy. As indicated, under extreme radiative forcing, the sunlit elements are much warmer than the shaded ones. The latter implies that accurate modelling of TOC emittance requires taking into account leaf level radiation balance and 3D canopy structure, either by explicit modelling of leaf level radiative processes or by parameterization. Thus, the sunlit and shaded elements need to be treated differently as,

$$B_\lambda(T_{b0}) = \sum_{i=1}^{4} f_i \varepsilon_i B_\lambda(T_i) \tag{3}$$

where: f_i , ε_i , and T_i are the fraction, emissivity, temperature of component element i, respectively. Totally, four elements, namely sunlit foliage, shaded foliage, sunlit soil and shaded soil are included. The equations for a four component system are derived in a similar way as shown here for two components [37].

The equations (2) and (3) do not account for the multiple interactions between canopy elements and soil which is the so-called cavity effect [69]. To simulate such a cavity effect, a non-linear item is introduced as [38,95]:

$$\begin{aligned} B(T_{b0}(\theta)) = {} & P(\theta)\varepsilon_s B(T_s) + [1-P(\theta)]\varepsilon_v B(T_v) + (1-P_h)\varepsilon_v B(T_v)P(\theta)(1-\varepsilon_s) \\ & + \alpha(1-\varepsilon_v)\varepsilon_v B(T_v)[1-P(\theta)] + \beta(1-\varepsilon_v)\varepsilon_s B(T_s)[1-P(\theta)] \\ & + (1-\varepsilon_c)R_{atm\downarrow} \end{aligned} \tag{4}$$

where $P(\theta)$ is the ground fractional cover viewed at angle $P(\theta) = 1 - f(\theta)$, ε_s and T_s are the soil emissivity and temperature, ε_v and T_v are leaf emissivity and temperature, P_h is the hemispheric gap frequency defined as the ratio of the radiation travelling through the canopy and reaching the soil to the incident radiation into the canopy over the hemisphere, α and β are respectively the probability of the radiation emitted by a leaf and reflected by other leaves in the canopy and the probability of the radiation emitted by soil and reflected by the leaves above it, ε_c is the canopy emissivity and $R_{atm\downarrow}$ is the downward hemispheric atmospheric radiance divided by π. The first term represents the proportion of the soil radiation that reaches the top of the canopy in the direction θ. The second term is the upward emitted radiation from the vegetation in the direction. The third term represents the downward radiation emitted by the vegetation and reflected by the soil and subsequently traveling upwards through the vegetation in the view direction, (vegetation-soil interaction). The fourth term is the contribution of the radiation emitted by the leaves towards other leaves into the canopy and reflected by these leaves towards outside the canopy in the view direction (vegetation-vegetation interaction). The fifth term is the contribution of the radiation emitted by soil towards the leaves and reflected by these leaves towards outside the canopy in the view direction (soil-vegetation interaction), The last term is the downward hemispheric atmospheric radiance reflected by the canopy system. If we define the effective emissivity of soil and vegetation, E_s and E_v, as:

$$E_s = \varepsilon_s + (1 - P_h)\varepsilon_v(1 - \varepsilon_s)\, B(T_v)/B(T_s) \tag{5a}$$

$$E_v = \varepsilon_v + \alpha(1 - \varepsilon_v)\varepsilon_v + \beta(1 - \varepsilon_v)\varepsilon_s\, B(T_s)/B(T_v) \tag{5b}$$

Eq. (4) is reduced to (2) with effective emissivity instead of actual emissivity.

5. Modeling of observations and sensor design

5.1 Modeling approach

The relationship between canopy geometry, leaf and soil properties, radiative and convective processes is rather complex (see previous Sections) leading to significant thermal heterogeneity, while radiometric measurements capture the overall effect of such heterogeneity only.

To understand the nature and information conveyed by radiometric measurements it is useful, therefore, to apply the modeling approach outlined in Sect. 4 to model observations and, particularly, their dependence on canopy (e.g. LAI) and soil (e.g. water content) properties [96]. Simulation of

radiometric data or full images can be done considering realistic canopy and environmental conditions by combining a soil-vegetation-atmosphere transfer (SVAT) model and atmospheric radiative transfer (RT) model [37].

Some TOC biophysical variables needed as input to the SVAT model are simulated using the RT models PROSPECT and GeoSAIL [97]. The TOC $T_b(\theta)$ was simulated using the SVAT model Cupid. Radiative transfer in the atmosphere is simulated using the RT model MODTRAN 4.0 taking into account the sensor specifications, particularly spectral coverage, spectral sampling and channel spectral response. The simulated images of directional radiance in two TIR channels (11 and 12 μm) at top-of-atmosphere (TOA) are obtained by adding the atmospheric effects to the top-of-canopy radiance (or images).

The SVAT model Cupid is a one-dimensional, multi-layer model that simulates various plant-environment interactions [98-100]. The essential processes simulated in the Cupid model are divided as above-ground processes and below-ground processes stratified by canopy layers (see figure 17).

Above-ground processes are dominated by vegetation including the transport of energy, mass and momentum between plants and their environment. Above-ground canopy is stratified by horizontal layers by identical increment of leaf area index and each horizontal vegetation layer is stratified by leaf angle class. Interactions between leaves in each individual leaf angle class in each horizontal layer and their local environment are first formulated. Collective effect of all the leaves in each horizontal layer is integrated to obtain the response of the layer. Canopy-level responses are simulated by numerical integration over all canopy layers where soil layers are also included.

The below-ground processes describe the transport of heat and mass between the roots and their soil environment and between the soil layers defined by identical increment of depth. Unlike many other SVAT models that take soil surface as lower boundary, Cupid has been developed to have plant root zone as the lower boundary. The soil lower boundary conditions consist of soil temperature and soil water content near the bottom of the root zone. All the processes occurring at the soil surface layer are simulated rather than input.

Leaf optical (reflectance, transmittance and emissivity) and physiological properties (photosynthetic rate, respiration rate and stomatal conductance) and leaf position and orientation arrangement determine energy and mass exchanges at leaf level, while canopy structure (leaf density distribution, total leaf area, and canopy height) determines the distribution of absorbed solar radiation in canopy layers thereafter determines mass and heat transfer between layers.

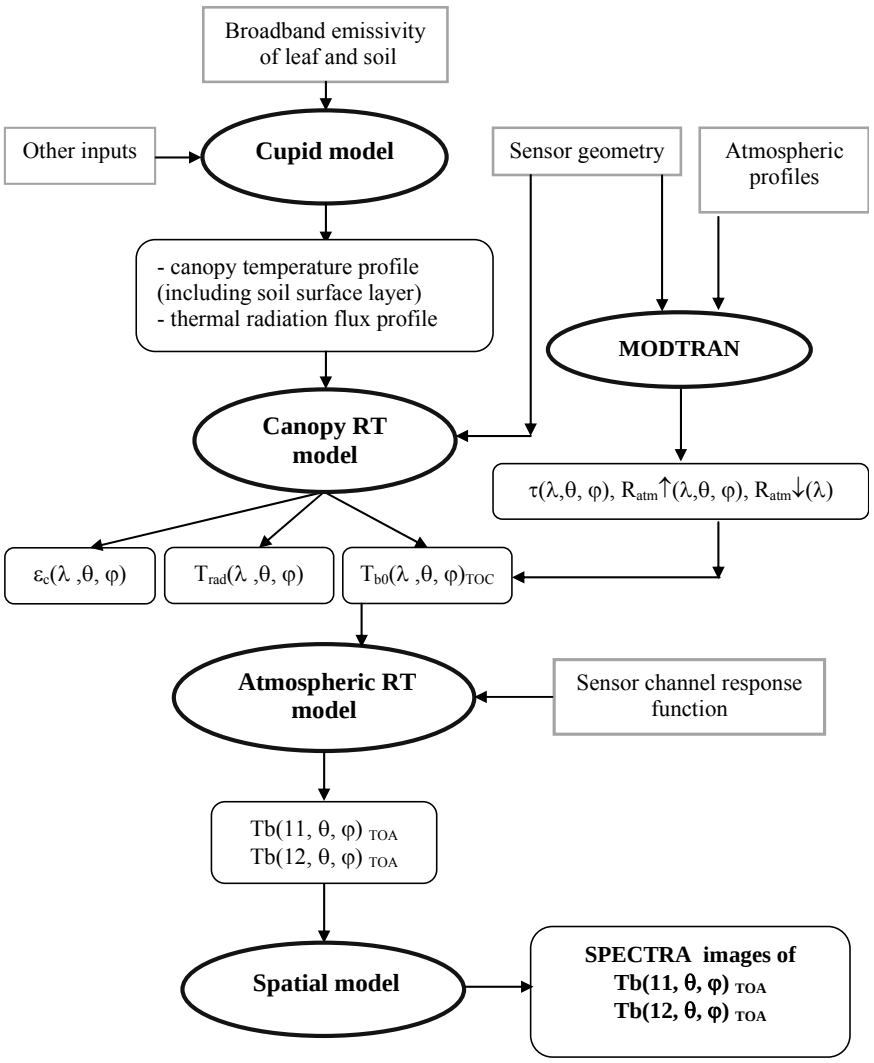

Figure 17. The major steps and applied models in the TIR image simulation [96].

The forcing of all the processes described in Cupid model is ambient atmospheric conditions above canopy and soil boundary conditions at the bottom of the root zone. Ambient atmospheric conditions are defined by solar radiation, air temperature, humidity, wind speed, and precipitation measured at some reference height above the canopy. Equations describing heat and mass throughout the entire canopy (leaf energy budget for all leaves and the vertical flux-gradient equations of soil and vegetation layers) are solved simultaneously. Among others canopy layer temperature profile (including soil surface layer) and thermal radiation flux profile are obtained from the solution of Cupid which can then be used to simulate canopy directional radiance in the concerned wavelength. This is done by assuming that the contributions of various leaf layers and of the soil layer are appropriately weighted by the

fraction of each layer viewed by the radiometer in a particular view direction. An overview of the simulation procedure is given in Figure 17.

5.2. Generation of synthetic multi-angular images

The at-sensor radiance is a combination of the surface-emitted radiance and the atmospheric contributions. The anisotropy of at-sensor radiance is due to atmospheric scattering, absorption and emission in addition to the inherent anisotropy of TOC radiance. The most significant interaction of TIR radiance with the atmosphere is attributed to atmospheric absorption primarily due to ozone and water vapor in the atmosphere. The optical path length is greater in the off-nadir views where the water vapor path increases, thus contributing higher upwelling atmospheric radiance, while atmospheric transmittance is smaller.

To demonstrate the approach described above a simulated data has been generated [96] for three European sites with a heterogeneous and detailed spatial structure to represent major, rather different biomes, such as evergreen forest, deciduous forest, savannah, semi – grasslands and agricultural land. Result presented here relate to two sites briefly described below:

1. Alpine Foreland site. The land surface is classified by 22 land use classes with grassland, mixed forest, shrubs, coniferous forest, deciduous forest, and various crops as dominant land cover types. Four dates were selected for image simulation: 22/04/2009, 17/06/2009, 19/07/2008, 18/09/2008. The central coordinates of these images are about 47.9 °N and 11.1 °E.

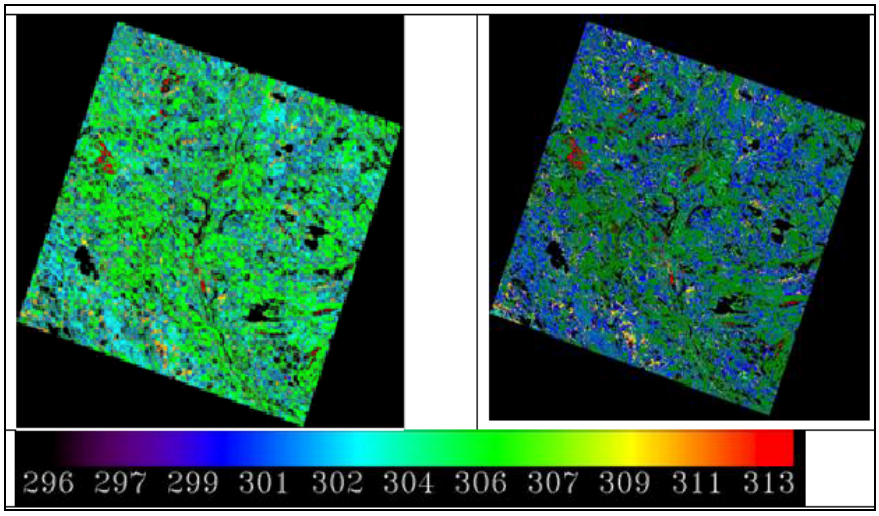

Figure 18. Synthetic multi-angular images of TOC $T_b(\theta)$; Boreal forest at Sodankyla, Finland: $\theta = 0°$ (left) and $\theta = +60°$ (right).

2. Boreal forest site. Boreal forest site is located in Sodankyla of Finland with typical boreal forest covered mainly by deciduous forest (ca. 42%) and coniferous forest (ca. 40%) and dark litter (ca. 12%). The soil in Sodankyla site is mainly sandy type.

After obtaining the atmospheric path radiance and transmittance using MODTRAN 4.0 in combining the atmospheric profiles at the two sites, the TOA TIR images were generated by applying these variables to the TOC TIR images. Figure 18 shows the images at the Sodankyla site as an example.

6. Retrieval algorithms

6.1 Introduction

An operational algorithm was described by [36] to retrieve soil and foliage component temperatures over heterogeneous land surface based on the analysis of bi-angular multi-spectral observations made by ATSR-2.

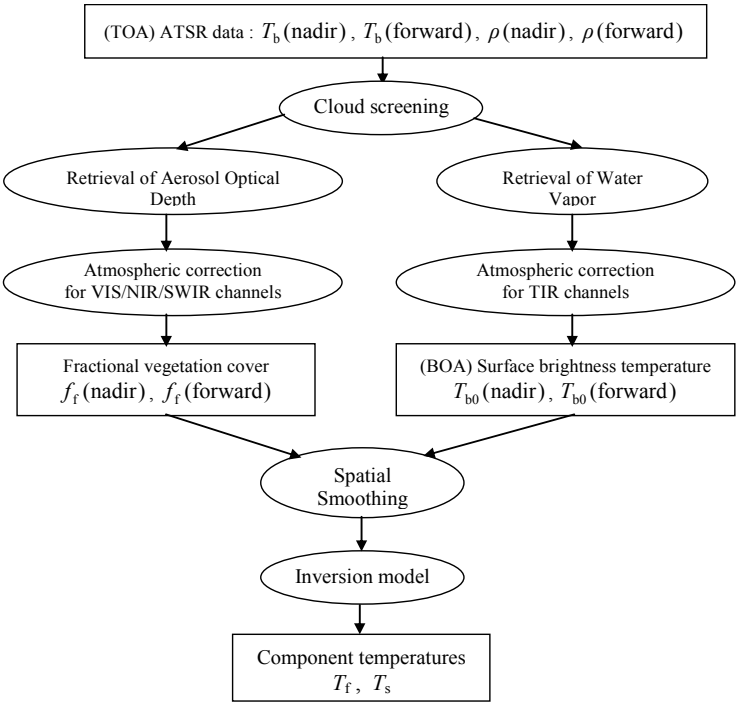

Figure 19. Scheme of the operational algorithm for retrieval of T_f and T_s from ATSR multi-spectral and dual-angular measurements. T_b is the brightness surface temperature at TOA measured by TIR channels of ATSR-2; ρ is reflectance at TOA measured by the VIS/NIR/SWIR channels of ATSR-2 (after [36]).

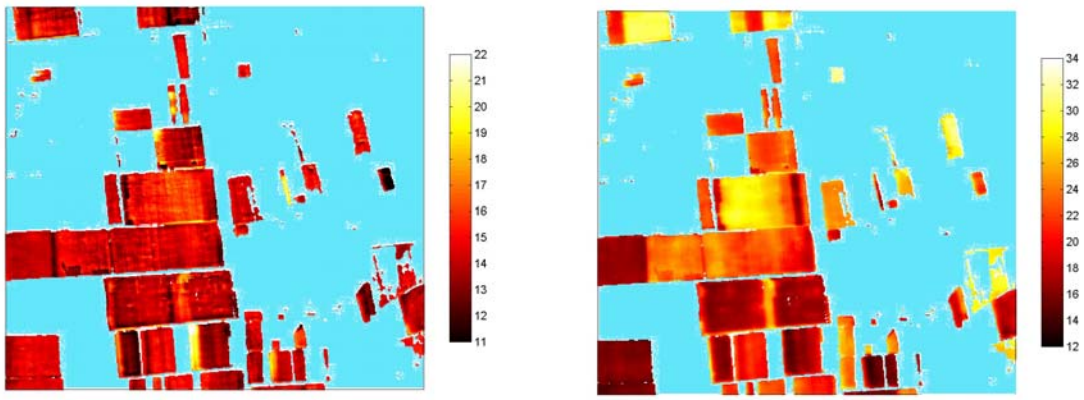

Figure 20. Foliage (left) and soil (right) component temperatures determined from AMTIS multi-angular measurements of exitance at 4200 m height; Shunyi experiment, China, April 2001 (after [40])

This algorithm is a good illustration of the synergistic use of multi-angular observations in the VNIR-SWIR region and in the TIR region to retrieve simultaneously both land surface and atmospheric variables (see also [101]). This algorithm is described in this section. On the basis of the radiative transfer theory in a canopy, a model is developed to infer the two component temperatures using six channels of ATSR-2. Four visible, near-infrared and short wave infrared channels are used to estimate the fractional vegetation cover within a pixel. A split-window method is developed to eliminate the atmospheric effects on the two thermal channels. An advanced method using all four visible, near-infrared and short wave channel measurements at two view angles is developed to perform atmospheric corrections in those channels allowing simultaneous retrieval of aerosol optical depth and land surface bi-directional reflectance (Figure 19).

This general approach has been applied to image data acquired with the airborne AMTIS (see Sect. 3). The algorithm was applied to retrieve foliage and soil temperatures of a winter wheat canopy [40]. since detailed ground measurements of component temperatures and of directional emittance were only available for this land cover type. Validation could, therefore, be done only for retrievals over winter wheat. All other land cover types were left out of consideration (light blue area in Figure 20).

6.2. Retrieval of $T_b(\theta)$ at TOC (top of canopy) from $T_b(\theta)$ at TOA (top of atmosphere)

Since the satellite measures the TOA brightness temperature (T), and the inversion of separate soil and vegetation temperature model needs the TOC

brightness temperature (T_{b0}), atmospheric corrections have to be performed. Moreover, since directional ground radiance (equivalent to ground brightness temperature) is likely to result from radiometric 3-D heterogeneity of the surface or the surface cover, neither a kinetic surface temperature nor an emissivity can be simply and uniquely defined [104], or even a value or angular behaviour assumed. Any separation between temperature and emissivity would rely on *a priori* assumptions or "definitions" of such variables. Thus, the first step in looking for directional effects is to consider the ground radiance as a whole. The consequence of that is that accurate atmospheric corrections have to be applied to TOA radiances (or brightness temperatures) in a given channel, preferably less affected by atmospheric perturbations, or, to say things differently, a common Split-Window method (SW) is not adequate (nor is a double angle method with (A)ATSR nadir/forward views). Indeed, a SW or similar regression algorithm for atmospheric corrections is designed to give the surface kinetic temperature, based on several assumptions regarding spectral and angular emissivity.

Single channel atmospheric correction is "just" inverting the radiative transfer equation integrated over the channel (i) bandwidth:

$$B_i(T_i) = B_i(T_{b0i})\,\tau_i + R_i^{atm}\uparrow \tag{6}$$

in order to get the ground radiance $B_i(T_{b0i})$, where T_{b0i} is the ground brightness temperature, T_i is the TOA measured brightness temperature, τ_i is the atmospheric transmission and $R_i^{atm}\uparrow$ is the atmospheric upward radiance. All quantities refer to a particular view direction, defined by zenith angle θ at ground level. The accuracy on $B_i(T_{b0i}(\theta))$ is determined by that on the atmospheric quantities, which in turn depends on the goodness of the radiative transfer code and the description of the vertical structure of the atmosphere. The second condition is by far the most important source of error. There is no simple parameterization allowing for determination of both τ_i and $R_i^{atm}\uparrow$. Atmospheric PTU profiles are needed.

Alternatively, if the ground brightness temperature is, or can be assumed, independent of the channels used to measure it, the Split Window (*SW*) [103, 104] method can be used to get T_{b0}. Following the procedure developed by [104], a general SW algorithm is derived for ATSR-2 nadir and forward views using simulated radiometric data [68]:

$$\begin{aligned} T_{b0}(\theta) = {} & \left[a(\theta) + b(\theta)W\right] + \left[c(\theta) + d(\theta)W\right]T_{11}(\theta) \\ & + \left[e(\theta) + f(\theta)W\right]\left[T_{11}(\theta) - T_{12}(\theta)\right] \end{aligned} \tag{7}$$

where θ. is view angle, W is the total column water vapor in the atmosphere. For the large range of surface parameters and atmospheric conditions ($W \le 4.5g/cm^2$, air temperature at surface T_a, 272K $\le T_a \le$ 311K and -5K $\le T_g$-$T_a \le$ 15K), the coefficients *a-f* have been generated for ATSR-2 nadir and forward views. They are *a*=-4.89, *b*=3.74, *c*=1.0205, *d*=-0.0151, e=0.916, f=0.509 the rms residual retrieval error $\sigma = 0.10$ K for the nadir image, and *a*=-14.41, *b*=8.51, *c*=1.0582, *d*=-0.0343, e=0.565, f=0.857 and σ =0.24 K for the forward view.

6.3. Retrieval of water vapor from ATSR-2 split-window channel data over land

Water vapor content in the atmosphere is required to improve the accuracy of the remotely sensed surface parameters [103, 50]. Nowadays, a number of different satellite approaches have been proposed and developed over the past two decades to measure atmospheric water vapor. According to the wavelength used, these approaches may be grouped into three categories: Near-infrared techniques [105,106]; Passive microwave techniques [107-109]; and Thermal infrared techniques [110-116].

Because the near-infrared technique is based on detecting the absorption by water vapor of the reflected solar radiation as it is transferred down to the surface and up through the atmosphere, use of this technique needs to have at least one channel in the water absorption band (0.94μm), and one nearby channel in the atmospheric windows (0.86 μm, 1.05μm and 1.24μm). Since ATSR-2 (Along-Track Scanner Radiometer) on board ERS-2 (European Remote Sensing) has only four channels in the visible and near infrared domain (0.55μm, 0.65μm, 0.87μm, 1.60μm) and three channels in the thermal infrared domain (3.7μm, 11μm and 12μm), no channel in the water absorption band is available, the near-infrared technique cannot be applied to ATSR2 data, the only one applicable technique is thermal infrared technique.

Up to now, there have been several attempts to derive water vapor using two split-window channels (11μm and 12μm). For instance, Kleespies and McMillin, [112] proposed a method based on the ratio of split-window channel brightness temperature differences assuming that the atmosphere and surface emissivities in the split-window channels are invariant. Jedlovec [113] proposed an extension of this concept and showed that the water vapor content can be derived using the ratio of the spatial variance of the channel brightness temperature. On the basis of these methods, Iwasaki [114] developed a new algorithm to reduce the non-linear effect of air temperature and unresolved cloud effect on the estimation of water vapor content using the split-window data. Sobrino et al. [116] improved Jedlovec [113] method by the use of Split-

Window Covariance-Variance Ratio (SWCVR). It has been shown that all these split-window methods are sensitive to instrument noise and are difficult to be applied to satellite data such as AVHRR in an operational manner [103,116]. Under the condition that the atmosphere and directional surface emissivity are constant or the effects of their spatial variations are not larger than the combined effects of both instrument noise over the *N* neighboring pixels, Li et al. [68] presented a new algorithm to determine quantitatively column water vapor content (W) directly from (A)ATSR Split–Window radiance measurements using the following formulae:

a) For ATSR2 nadir view:

$$W = 13.73 - 13.662\,\tau_j / \tau_i \tag{8}$$

where the subscripts i, j denote respectively channel 11μm and channel 12μm of ATSR.

b) For ATSR2 forward view ($\theta \cong 53°$):

$$W = 10.02 - 9.971\,\tau_j / \tau_i \tag{9}$$

with

$$\frac{\tau_j}{\tau_i} = \frac{\varepsilon_i}{\varepsilon_j} R_{ji} \quad \text{with } R_{ji} = \frac{\sum_{k=1}^{N} (T_{i,k} - \overline{T_i})(T_{j,k} - \overline{T_j})}{\sum_{k=1}^{N} (T_{i,k} - \overline{T_i})^2} \tag{10}$$

in which the subscript *k* denotes pixel *k*, $T_{i,k}$ and $T_{j,k}$ are the brightness temperatures of pixel k in channels i and j measured at satellite level, respectively, $\overline{T_i}$ and $\overline{T_j}$ are the mean (or the median) brightness temperatures of the *N* neighboring pixels considered, respectively.

This method was developed and applied to several ATSR2 data sets. The water vapor contents retrieved using ATSR2 data from SGP'97 (USA), Barrax (Spain) and Cabauw (The Netherlands) are in good agreement with those measured by the quasi-simultaneous radiosonde. The mean and the standard deviation of their difference are respectively 0.04 and 0.22 g/cm^2. It is shown that water vapor content derived from ATSR2 data using the proposed algorithm is accurate enough in most cases for surface temperature determination with split-window technique using ATSR2 data and for

atmospheric corrections in visible and near-infrared channels of ATSR2. A more detailed description of this method and its applicability can be found in [68].

6.4. Retrieval of aerosol optical depth from ATSR-2 data for atmospheric corrections

Atmospheric perturbations (mainly due to absorption and scattering processes) are responsible for substantial modifications of the surface spectral reflectance measured by satellite instruments. It is therefore necessary to correct the atmospheric effects to retrieve the surface reflectance. Methods of atmospheric corrections are generally concerned with the estimation of the atmospheric effects associated with molecular absorption, molecular and aerosol scattering. Current methods for the estimation of the atmospheric effects employ a radiative transfer model [117,118] whose inputs are generally the vertically integrated gaseous contents, aerosol optical properties and geometric conditions.

If ρ_i^* is the reflectance measured in channel i at the top of atmosphere (TOA), from radiative transfer theory, the surface reflectance in channel i, ρ_i, can be expressed as [117,119]:

$$\rho_i(\theta_S, \theta_\upsilon, \Delta\phi) = \frac{\rho_i^{ac}(\theta_S, \theta_\upsilon, \Delta\phi)}{1 + S_i \rho_i^{ac}(\theta_S, \theta_\upsilon, \Delta\phi)} \tag{11}$$

with

$$\rho_i^{ac} = \frac{\rho_i^*(\theta_S, \theta_\upsilon, \Delta\phi) \Big/ tg_i(\theta_S, \theta_\upsilon) - \rho_i^a(\theta_S, \theta_\upsilon, \Delta\phi)}{t_i(\theta_S) t_i(\theta_\upsilon)}$$

where θ_s and θ_υ are solar and viewing zenith angles, respectively. $\Delta\phi$ is the relative azimuth between sun and satellite direction. S_i is the spherical albedo of atmosphere in channel i. tg_i is the total gaseous transmission in channel i associated with gaseous absorption along the sun-target-sensor atmospheric path. $\rho_i^a(\theta_s, \theta_\upsilon, \Delta\phi)$ is the atmospheric reflectance. $t_i(\theta_s)$ and $t_i(\theta_\upsilon)$ are the total atmospheric scattering transmittance along the sun-target and target-sensor atmospheric paths, respectively.

In general, the independent measurements of atmospheric composition and aerosol optical properties are not available; it is therefore desirable to derive them directly from satellite data. The most important gases in atmospheric corrections in visible and near infrared channels are water vapor and ozone.

Water vapor content in the atmosphere may be derived from the two split-window channel measurements as shown above, and ozone content is taken from climatological data. As for the determination of the aerosol optical properties, if the surface reflectance may be considered isotropic, then the difference in surface reflectance retrieved from multi-angle directions using equation (1) may be used to derive the atmospheric optical thickness if aerosol type is assumed. However, most land surfaces are far from Lambertian [120]. With multi-angle measurements, it is imperative to consider non-Lambertian reflectances. Several multi-look aerosol retrieval schemes for ATSR-2 have been proposed [121-123]. The iteration of a two step-process proposed by [123] can be used. The first step is to derive using eq. (1) eight land surface reflectances $\rho_i(\theta_s,\theta_v,\Delta\phi)$ from the TOA reflectance ρ^* made at four channels (0.55 μm, 0.65 μm, 0.87 μm, 1.60 μm) and two view angles (nadir and forward views), given an initial estimate of the atmospheric aerosol and optical depth at 550nm (τ_{550}^a). The second step is to fit land surface bi-directional reflectance model to eight retrieved surface reflectances by the minimization of the error metric function:

$$E=\sum_{\theta_v=1}^{2}\sum_{i=1}^{4}\left[\rho_i(\theta_s,\theta_v,\Delta\phi)-\rho_i^m(\theta_s,\theta_v,\Delta\phi)\right]^2 \tag{12}$$

where $\rho_i^m(\theta_s,\theta_v,\Delta\phi)$ is the land reflectance in channel I predicted by the reflectance model.

Since there are maximum eight land surface reflectance measurements, land surface bi-directional model must have maximum seven free model parameters so that there is at least one degree of freedom available for atmospheric parameter retrieval, for instance, the aerosol optical depth (τ_{550}^a). Considering the land surface to be composed of opaque facets, each with Lambertian reflectance ω_i, and separating parameters relating to the wavelength invariant three-dimensional structure of the surface from wavelength dependent parameters describing the component spectra, [123] developed a seven free parameter (*P* nadir, *P* forward, γ and ω_i (*i*=1,4)) model as:

$$\begin{aligned}\rho_i(\theta_S,\theta_V,\Delta\phi)&=(1-D_i)P(\theta_S,\theta_V,\Delta\phi)\omega_i\\&+\frac{\gamma\omega_i}{1-(1-\gamma)\omega_i}\left[D_i+(1-\gamma)\omega_i(1-D_i)\right]\end{aligned} \tag{13}$$

where D_i is the incident diffuse fraction which excludes the radiation scattered close to the solar beam direction. D_i can be estimated by radiative transfer model for solar direction and aerosol optical depth. $P(\theta_S,\theta_V,\Delta\phi)$ is the

geometric parameter dependent only on view and illumination directions. γ denotes the mean hemispherically integrated probability of escape of light without further interaction, after a scattering event at the land surface.

In case where there are no four channels available, an alternative scheme can be used to retrieve the aerosol optical depth by assuming that the functional shape of the bidirectional effects is invariant with respect to the wavelength within the visible and near-infrared region [120,121], namely:

$$\frac{\rho_i(\theta_s,\theta_{\upsilon 1},\Delta\phi)}{\rho_i(\theta_s,\theta_{\upsilon 2},\Delta\phi)}=\frac{\rho_j(\theta_s,\theta_{\upsilon 1},\Delta\phi)}{\rho_j(\theta_s,\theta_{\upsilon 2},\Delta\phi)} \tag{14}$$

This relationship gives a constraint for atmospheric correction by forcing the retrieved bidirectional reflectance to have a consistent angular variation, even thought the magnitude of the reflectance may vary greatly.

The aerosol optical thickness is therefore obtained through the minimization of the error metric function:

$$E=\sum_{i=1}^{n}\sum_{j>i}^{n}\left[\frac{\rho_i(\theta_s,\theta_{\upsilon 1},\Delta\phi)}{\rho_i(\theta_s,\theta_{\upsilon 2},\Delta\phi)}-\frac{\rho_j(\theta_s,\theta_{\upsilon 1},\Delta\phi)}{\rho_j(\theta_s,\theta_{\upsilon 2},\Delta\phi)}\right]^2 \tag{15}$$

where n is the total number of channels available, i and j are channel numbers. The details of these methods can be found in [123].

6.5. Retrieval of vegetation fractional cover

To retrieve soil and foliage temperatures from equation 2 or 4, the viewing angle-dependent vegetation fraction needs to be determined independently from additional observations, such as the TOC reflectances in the VNIR and SWIR spectral channels of ATSR-2 and AATSR. The approach presented here is an example, while for a review on retrieval of fractional cover, see e.g. [123]. The approach to estimate the fractional vegetation cover uses visible and near infrared data.

A stepwise multiple linear regression were applied in this study to estimate the fractional vegetation cover $f_{\mathrm{f}}(\theta_{\mathrm{v}})$ using TOC reflectances $\rho_{\mathrm{i}}(\theta_{\mathrm{S}},\theta_{\mathrm{V}},\Delta\varphi)$. The stepwise multiple linear regression is written

$$f_{\mathrm{f}}(\theta_{\mathrm{V}}) \;=\; a_0(\theta_{\mathrm{S}},\theta_{\mathrm{V}})+\sum_{i=1}^{n}a_{\mathrm{i}}(\theta_{\mathrm{S}},\theta_{\mathrm{V}})\rho_{\mathrm{i}}(\theta_{\mathrm{S}},\theta_{\mathrm{V}},\Delta\varphi) \tag{16}$$

where *n* is the number of channels used.

The model OSCAR [124] has been applied to generate surface reflectances for the viewing and illumination conditions applying to the ATSR-observations used in this study and to an ensemble of canopy and atmospheric conditions. This synthetic data base, where f_f is known for any given canopy condition, has been used to determine the coefficients a_i in Eq. 16. A different set of coefficients is obtained for each viewing geometry (see also [37]).

6.6. Conclusions

Vegetation fractional cover. The regression model (Eq.16) works rather well when vegetation is green, i.e. corn and alfalfa, while slightly larger errors appear for vegetation with some fraction of brown leaves, like barley at this time of the year (DOY = 179). Table 3 gives the summary of the model performance represented by RMSE and Absolute Difference (AD) for each case and for the total dataset.

Retrieval of soil and foliage component temperatures. The validation of the retrieved component temperatures using ATSR-2 bi-angular measurements is challenging due to the difficulty of obtaining observations of temperatures of soil and foliage in situ at ATSR-2 spatial resolution (i.e. 1.5 km x 2.5 km) for the forward view.

As done to evaluate the algorithm for $f_f(\theta_v)$, the same method, i.e. using synthetic radiometric data generated with detailed modelling of radiative transfer in the soil-vegetation-atmosphere system and inversion using a simplified algorithm (suitable for operational processing of actual data), can be used to evaluate the retrievals of T_f. The reference T_f and T_s were simulated using the complete model CUPID and the TOC radiance was calculated (for each image pixel) with the procedure outlined Sect. 6.5. The $T_{b0}(\theta_v, \varphi_v)$ at $\theta_v = 0°$ and $\theta_v = 53°$ obtained in this way were then treated as observations in Eq. 4 to retrieve T_f and T_s. The comparisons between the retrievals and the simulations of T_f and T_s for the three crops are encouraging (Table 4).

Table 3. The performance of the regression equation for estimating fractional vegetation cover (Eq. 16) as presented by RMSE and AD at nadir and forward 53° for each vegetation type. 'Total' indicates the overall performance over the entire simulation dataset.

Vegetation	$\theta_v = 0°$		$\theta_v = 53°$	
	RMSE	AD	RMSE	AD
Corn	0.0339	0.025	0.1038	0.103
Barely	0.1086	0.109	0.0745	0.073
Alfalfa	0.0327	0.030	0.0515	0.049
Total	0.0456	0.046	0.0785	0.076

Table 4. RMSE between retrieval and simulation of T_f and T_s for corn, barley and alfalfa crops.

	Corn	Barley	Alfalfa
RMSE of T_f	0.381905	1.164064	0.590805
RMSE of T_s	0.669429	0.867213	0.772624

7. Limitations of current systems and perspectives

Over the last 25 years measurements of emittance by goniometer-mounted radiometers has been the main source of observations to document and understand the anisotropic emittance of vegetation canopies. This experimental body of knowledge led to the development of detailed models of the complex processes which determine the significant thermal heterogeneity of the canopy space. The latter is of particular relevance towards a better understanding of the relation between canopy architecture and foliage–atmosphere exchanges of radiation, water and carbon.

On the other hand, the capability of goniometer-mounted radiometers is severely limited both as regards the size of targets and sampling of the spatial variability. Actual exploitation of the unique information conveyed by anisotropic emittance requires imaging radiometers to sample sufficiently large terrestrial targets at a spatial resolution sufficiently large to integrate emitted radiance over an area representative of the target, but sufficiently small to provide independent observations of different land cover types.

The ATSR series of instruments is the only current observing system providing directional (at two view angles) observations of emittance and these observations have been used to demonstrate the relevance of directional measurements in the TIR region. (see e.g. [95, 126,127]). On the other hand, the large footprint of (A) ATSR and even more the large difference in footprint between the nadir and forward view, make validation of data products very challenging and restrict applications to large scale modeling. For example, the difference between foliage and soil temperature might be used as a measure of drought or crop water stress, but given the low resolution is difficult to relate to the spatial scale of crop and water management practices.

The European Space Agency had been studying a high spatial resolution mission for multi-angular land observations (SPECTRA, see [128]), but this project has been abandoned. The Italian Space Agencies (ASI) is developing an Earth Observation mission with similar characteristics [129] with expected launch in 2012. The latter would provide simultaneous VNIR – SWIR hyper-spectral and multi-spectral observations at high spatial resolution and is being designed specifically for land observations.

In general terms, multi-angular measurements of TIR emittance over land provide access to radiative and convective processes in the canopy space which concur to determine the response of terrestrial vegetation to environmental forcing.

Acknowledgements

Work by the Authors summarized in this chapter has been funded by the European Space Agency (Contracts 13177/98NL/GD; 15164/01/NL/SF; 17169/03/NL/GS; 17179/03/NL/GS), the European Commission (Contracts FP6 GMES no. 502057, FP5 MIND EVK2-CT-2002-00158), the Netherlands Users Support Program (GO-2 Contract SRON EO-049.) and the Italian Space Agency (ASI Contract ASI I/R/073/01). The Shunyi field campaign was part of the 'Quantitative of Remote Sensing theory and application for Land Surface Parameters (QRSLSP)' project funded by China's Ministry of Science and Technology Funds for Major State Basic Research (project No. G2000077900, led by Prof. X. Li). Dr. Qiang Liu is thanked for the data processing of goniometer and AMTIS measurements.

References

1. Bowen, I.S., 1926, The ratio of heat losses by conduction and by evaporation from any water surface, Physics Review Vol.27: 779-787.
2. Monteith, J. L., 1965, Evaporation and environment, In: The State and Movement of Water in Living Organisms, G.E. Fogg (ed.), Sympos. Soc. Exper. Biol., Academic Press, N.Y., 19: 205-234.
3. Feddes, R.A., 1971, Water, heat and crop growth, PhD. Thesis, Wageningen, Agricultral University, The Netherlands. H. Veenman & Zonen, Wageningen: 184 p.
4. Verma, S.B, Rosenberg, N.J., Blad, B.L. and Baradas, N.W., 1976, Resistance-energy balance method for predicting evapotranpiration, determination of boundary layer resistance, and evaluation of error effects, Agronomy Journal, 68: 776-782.
5. Hall, A.E., Canell, G.H., and Lawton, H.W., 1979, Agriculture in semi-arid environments, Springer-Verlag Berlin Heidelberg New York, 340pp.
6. Prince, J.C., 1982, On the use of satellite data to infer surface fluxes at meteorological scales. J. Appl. Meteorol. Vol. 21: 1111-1122.
7. De Bruin, H.A.R., and C.M.J. Jacobs, 1989. Forest and regional scale processes. Phil. Trans. R. Met Soc. Vol.B 324: 393-406.
8. Beljaars, A.C.M., and Holtslag, A.A.M., 1991, Flux parameterization over land surface for atmospheric models, J. Appl. Meteorol., 30: 327-341.
9. Lhomme, J.-P., Monteny, B., Chehbouni, A., Troufleau, D., 1994b, Determination of sensible heat flux over Sahelian fallow savannah using infra-red thermometry, Agric. For. Meteorol., 68: 93-105.

10. Sellers P.J., D.A.Randall, G.J, Collatz, J.A. Berry, C.B. Field, D.A.Dazlich, C. Zhang, G.D. Colleli and L.Bounoua, 1996. A Revised land surface parameterization (SIB2) for atmopsheric GCMS. Part 1: Model formulation. J.Climate Vol.9(4): 676-705.
11. Blad, B.L., and N.J. Rosenberg, 1976. Evaluation of resistance and mass transport evapotranspiration models requiring canopy temperature data, Agronomy Journal, 68: 764-769.
12. Seguin, B., E.Assad, J. P.Freteaud, J. Imbernon, Y.H. Kerr and J.P. Lagouarde, 1989, Use of meteorological satellite for water balance monitoring in Sahelian regions. Int. J. Remote Sens. Vol. 10: 1001-1017.
13. Hatfield, J.L., R.J. Reginato and S. B. Idso, 1984. Evaluation of canopy temperature – evapotranspiration models over various crops. Agric. Meteorol. Vol. 32: 41-53.
14. Jackson, R.D., S.B. Idso, R.J.Reginato and P.J.Pinter, 1981. Canopy temperature as a Crop Water Stress Indicator. Water Resources Research Vol. 17(4): 1133-1138.
15. Menenti, M. and B. J. Choudhury, 1993, Parameterization of land surface evapotranspiration using a location- dependent potential evapotranspiration and surface temperature range. In: H.J. Bolle et al. (Eds.). Exchange processes at the land surface for a range of space and time scales, IAHS Publ. 212: 561-568.
16. Moran, M.S., T.R.Clarke, Y. Inoue and A.Vidal, 1994. Estimating crop water deficit using the relation between surface air temperature and spectral vegetation index. Rem. Sens. Environ. Vol. 49(3): 246 263.
17. Jackson, R.D., 1985. Evaluating evapotranspiration at local and regional scales. Proc. IEEE Vol. 73: 1086-1095.
18. Huband, N.D.S., and J.L. Monteith, 1986. Radiative surface temperature and energy balance of a wheat canopy. Boundary-Layer Meteorol. Vol. 36: 1-17.
19. Choudhury, B.J., R.J. Reginato, and S.B. Idso, 1986, An analysis of infrared temperature observations over wheat and calculation of the latent heat flux, Agric. For. Meteorol., 37: 75-88.
20. Mahfouf, J. F., E. Richard and P. Mascart, 1987. The influence of soil and vegetation on the development of mesoscale circulations. J. Clim. Appl. Meteor. Vol. 26, 1483-1495
21. Segal, R. Avissar, M. C. McCumber and R. A. Pielke, 1988. Evaluations of vegetation effects on the generation and modification of mesoscale circulations. J. Atmos. Sci. Vol. 45: 2268-2292.
22. Hatfield, J. L., 1991. Development of agricultural crops and practices adapted to arid land conditions, 1991. Proc. SCS multiconference on AI simulation: Agricultural crops and practices adapted to arid lands. University of New Mexico Press: 39-60.
23. Xue, Y., and J. Shukla, 1993. The influence of land surface properties on Sahel climate. Part I: Desertification. J. Climate Vol. 6: 2232–2245.
24. Wang, J. and Y. Mitsuta, 1992. An observation study of turbulent study of turbulent structure and transfer characteristics in Heihe oasis. J. Meteor. Soc. Japan Vol. 70: 1147-1154.

25. Avissar, R. and R.A. Pielke, 1989. A parameterization of heterogeneous land-surface for atmospheric numerical models and its impact on regional meteorology. Mon. Wea. Rev. Vol.117:2113-2136.
26. Pielke, R.A., G.Dalu and J.S. Snook et al., 1991. Nonlinear influence of mesoscale land use on weather and climate. J. Climate Vol. 4: 1053-1069.
27. Peng, X.D and L.S., Cheng, 1993. Numerical simulations of the PBL mean structure and fluxed in HEIHE region. Proceedings of International Symposium on HEIFE. Kyoto University, Kyoto, Japan: 437-442.
28. Yan, Y., 1999. Numerical simulation of land surface process on heterogeneous surface. PhD Dissertation. Lanzhou Institute of Plateau Atmospheric Physics. Chinese Academy of Sciences: 90 p.
29. Balick, L. K., B.A. Hutchison, J.A. Smith and M.J. McGuire, 1987. Directional thermal exitance distributions of a deciduous forest in summer. IEEE Trans. Geosci. Remote Sensing Vol. 25: 410-412.
30. Kimes, D.S. and J.A. Kirchner, 1983. Directional radiometric measurements of row-crop temperatures. Int. J. Remote Sens. Vol. 4(2): 299-311.
31. Qualls, R.J. and D.N.Yates, 2001. Directional radiometric temperature profiles within a grass canopy, Adv. in Water Resources, 24: 145-155.
32. Norman, J.M. and J.L. Chen, 1990. Thermal emissivity and infrared temperatures dependence on plant canopy architecture and view angle. in Proceedings of the International Geoscience and Remote Sensing Symposium (IGARSS'90, IEEE Geoscience and Remote Sensing Society, New York, NY, USA): 1747-1750.
33. Otterman, J., 1990. Inferring parameters for canopies non uniform in azimuth by model inversion. Rem. Sens. Environ. Vol. 33: 41-53.
34. Smith, J.A. and S. M. Goltz, 1995. A thermal exitance and energy balance model for forest canopies. IEEE Trans. Geosci. Rem. Sens. Vol. 32(5): 1060-1066.
35. Francois, C.,C. Ottle and L. Prevot, 1997. Analytical parameterization of canopy directional emissivity and directional radiance in thermal infrared. Application on the retrieval of soil and foliage temperatures using two directional measurements. Intern. J. of Rem. Sens. Vol. 18(12): 2587-2612.
36. Jia, L., Z.-L. Li, M. Menenti, Z.-B Su, W. Verhoef and Z.-M Wan, 2003. A practical algorithm to infer soil and foliage component temperatures from bi-angular ATSR-2 data. Int. J. Remote Sensing Vol. 24(23): 4739–4760.
37. Jia, L., 2004. Modeling heat exchanges at the land-atmosphere interface using multi-angular thermal infrared measurements. Wageningen University, ISBN 90-8504-041-8: 199 p.
38. Li, Z.-L., M.P. Stoll, R.H. Zhang, L. Jia and Z. Su, 2001. On the separate retrieval of soil and vegetation temperatures from ATSR2 data. Science in China, Series D Vol. 44(2): 97-111.
39. Francois, C., 2002. The potential of directional radiometric temperatures for monitoring soil and leaf temperature and soil moisture status. Remote Sens. Environ. Vol. 80: 122– 133.
40. Liu, Q., 2002. Study on Component Temperature Inversion Algorithm and the Scale Structure for Remote Sensing Pixel. PhD dissertation of Chinese Academy of Sciences.: 111 p.

41. Luquet, D., A. Bégué, A. Vidal, P. Clouvel, J. Dauzat, A. Olioso, X.-F. Gu and Y. Tao, 2003. Using multidirectional thermography to characterize water status of cotton. Rem. Sens. Environ. Vol. 84: 411-421.
42. Field, C.B. and H.A. Mooney, 1986: The photosynthesis – nitrogen relationship in wild plants. In: T.J. Givnish (Ed.) On the Economy of Plant Form and Function. Cambridge. Univ. Press. New York, USA: 25 –55.
43. Medlyn B.E., E. Dreyer, D.S. Ellsworth, M. Forstreuter, P.C. Harley, M.U. F. Kirshbaum, X. Le Roux, P. Montpied, J. Strassemeyer, A. Walcroft, K. Wang, D. Loustau, 2002. Temperature response of parameters of a biochemically-based model of photosynthesis. II. A review of experimental data. Plant, Cell and Environment, Vol. 25: 1167–1179.
44. Valentini, R., A.J.Dolman, P.Ciais, Schulze E.D., A.Freibauer, D.S.Schimel and M.Heimann, 2000. Accounting for carbon sinks in the biosphere, European perspective. CARBOEUROPE European Office. Max-Planck Institute for Biogeochemistry, P.O. Box 100164. 07700 Jena, Germany: 17p.
45. Matteucci G., S. Dore, S. Stivanello, C. Rebmann and N. Buchmann, 2000. Soil respiration in beech and spruce forests in Europe: Trends, controlling factors, annual budgets and implications for the ecosystem carbon balance. in: E.D, Schulze (Ed.): Carbon and Nitrogen Cycling in European Forest Ecosystems. Vol. 142. Springer, Berlin: 217-236.
46. Becker, F., 1987, The impact of spectral emissivity on the measurement of land surface temperature from a satellite, Intern. J. of Rem. Sens., Vol. 8: 1509-1522.
47. Becker,F.P. Ramanantsizehena, and M.-P. Stoll, 1985, Angular variation of the bidirectional reflectance of bare soils in the thermal infrared band. Appl. Opt. Vol. 24 (3): 365-375.
48. Labed, J. and M. P.Stoll, 1991. Spatial Variability of Land Surface Emissivity in the Thermal Infrared Band: Spectral Signature and Effective Surface Temperature. Rem. Sens. Environ. Vol.38: 1-17.
49. Masuda, K., T. Takashima and Y. Takayama, 1988. Emissivity of pure and sea waters for the model sea surface in the infrared window regions. Rem. Sens. Environ. Vol. 313-329.
50. Francois, C. and C. Ottle, 1996. Atmospheric corrections in the thermal infrared: global and watervapor dependent split-window algorithms-applications to ATSR and AVHRR data. IEEE Trans. Geosc. and Rem. Sens. Vol. 34(2): 457-470.
51. Nerry, F.J. Labed and M.-P. Stoll, 1988, Emissivity signatures in the thermal IR band for remote sensing: calibration procedure and method of measurement, Appl Opt. Vol. 27, No.4: 758-764.
52. Petitcolin, F., F. Nerry and M. P.Stoll, 2002. Mapping Temperature Independent Spectral Indice of Emissivity and directional emissivity in AVHRR channels 4 and 5. Int. J. Remote Sens. Vol. 23(17): 3473 – 3491.
53. Sobrino, J.C. and J. Cuenca, 1999, Angular variation of thermal infrared emissivity for some natural surfaces from experimental measurements. Appl. Opt. Vol. 38 (18): 3931-3936.

54. Snyder W.C., Z.-M. Wan, Y. Zhang and Y.-Z Feng, 1997. Thermal Infrared (3-14 μm) Bidirectional Reflectance Measurements of Sands and Soils. Rem. Sens. Env. Vol. 60(1): 101-109.
55. Kimes, D.S., 1980. Effects of vegetation canopy structure on remotely sensed canopy temperatures. Rem. Sens. Env. Vol. 10: 165-174.
56. Albertson, J., G. Katul, and P. Wiberg, 2001. Relative importance of local and regional controls on coupled water, carbon, and energy fluxes. Advances in Water Resources Vol. 24: 1103–1118.
57. Wilson, K, A. Goldstein, E. Falge, M. Aubinet, D. Baldocchi, P. Berbigier, C.Bernhofer, R. Ceulemans, H. Dolman, C. Field, A. Grelle, A. Ibrom, B.E. Law, A. Kowalski, T. Meyers, J. Moncrieff, R. Monson, W. Oechel, J. Tenhunen, R. Valentini and S. Verma, 2002. Energy balance closure at FLUXNET sites. Agric. For. Meteorol. Vol. 113(1-4): 223 – 243.
58. Paw U, K.T., S.L.Ustin, , and C.A. Zhang,., 1989, Anisotropy of thermal infrared exitance in sunflower canopies, Agric. Forest Meteorol. Vol. 48: 45-58.
59. Lei, S.A., 2004. Leaf temperatures of Blackbrush: relationships with air and soil surface temperatures. USDA Forest Service Proceedings RMRS-P-31.
60. Nielsen, D.C., K. L. Clawson and B. L. Blad, 1984. Effect of solar azimuth and infrared thermometer view direction on measured soybean canopy temperature. Agronomy Journal Vol. 76: 607-610.
61. Jackson, R.D. and S. B. Idso, 1975. Surface albedo and desertification. Science Vol.189: 1012-1013.
62. Lagouarde, J.P., Y.H. Kerr and Y. Brunet, Y., 1995, An experimental study of angular effects on surface temperature for various plant canopies and bare soils. Agric. For. Meteorol. Vol. 77: 167-190.
63. Zhang R.-H., X.-M Sun. H.-B. Su, Z.-L Zhu and X.-Z. Tang, 2002. A new design for measuring directional radiant temperature and data analysis. Proc. IEEE 2002 Int. Geoscience and Rem. Sens. Symposium (IGARSS'02) Vol. V: 2768-2770.
64. Li, Z.-L., R.-H Zhang, X.-M Sun, H.-B. Su, X.-Z. Tang, Z.-L Zhu and J.A.Sobrino, 2004. Experiment system for the study of the directional thermal emission of natural surfaces. Int. J. Remote Sens. Vol. 25(1): 195-204.
65. Liu, Q.H., Xiaowen Li X.W. and L.F. Chen, 2002. Field Campaign for Quantitative Remote Sensing In Beijing. Proc. IEEE 2002 International Geoscience and Remote Sensing Symposium (IGARSS'02). Vol. VI: 3133-3135.
66. Wang, J., F. Yan, J. Xiao, T. Wei and J. Wang, 2002, Development of an Airborne Multi-angle TIR/VNIR Imaging System. IEEE 2002 International Geoscience and Remote Sensing Symposium (IGARSS'02) Vol., IV: 2245-2248.
67. Mutlow, C.T., A.M. Závody,. I.J. Barton and D.T. Llewellyn-Jones, 1994. Sea surface temperature measurements by the along-track scanning radiometer on the ERS 1 satellite: Early results. J. Geophys. Res.. Vol. 99 (C11): 22575-22588.
68. Li Z.-L., Jia L., Su Z, Wan Z and Zhang R.-H, 2003. A new approach for retrieving precipitable water vapour from ATSR2 split-window channel data over land area. Intern. J. of Rem. Sens. Vol.24: 5095-5117.

69. Sutherland, R. A. and Bartholic, J. F., 1977. Significance of vegetation in interpreting thermal radiation from a terrestrial surface. J. Appl. Meteorol. Vol.18, 759-763
70. Kimes, D.S., J.A. Smith and L.E. Link, 1981. Thermal IR exitance model of a plant canopy. Appl. Opt. Vol. 20(4): 623-632
71. Kimes, D.S., 1983. Remote sensing of row crop structure and component temperatures using directional radiometric temperatures and inversion techniques. Rem. Sens. of Env. Vol. 13: 33-55
72. Sobrino J.A. and Caselles V.,1990. Thermal infrared model for interpreting the directional radiometric temperature of a vegetative surface. R em. Sens. of Env. Vol.33:193-199
73. Caselles, V., J.A. Sobrino and C. Coll, 1992. A physical model for interpreting the land surface temperature obtained by remote sensors over incomplete canopies. Remote Sens. Environ. Vol. 39: 203-211
74. Colton, A.L., 1996. Effective thermal parameters for a heterogeneous land surface. Remote Sens. Environ. Vol. 57: 143-160
75. Otterman, J., T.W. Brakke and J. Susskind, 1992. A model for inferring canopy and underlying soil temperatures from multi-direcitonal measurements, Boundary-layer Meteorol. Vol.61: 81-97
76. Otterman, J., J. Susskind, T. Brakke, D Kimes, R. Pielke and T.J. Lee, 1995. Inferring the thermal-infrared hemispheric emission from a sparsely-vegetation surface by directional measurement, Boundary-layer Meteorol. Vol.74:163-180
77. Ottermann, J., T.W. Brakke, M. Fuchs, V. Lakshmi and M. Cadeddu, 1999. Longwave emission from a plant/soil surface as a function of the view direction: Dependence on the canopy architecture. . Int. J. Remote Sens. Vol. 20 (11): 2195-2201
78. McGuire, M.J., J.A.Smith, L.K. Balick and B.A. Hutchison, 1989. Modeling directional thermal radiance from a forest canopy. Rem. Sens. Environ. Vol. 27: 169-186
79. Kimes, D.S., 1981. Remote sensing of temperature profiles in vegetation canopies using multiple view angles and inversion techniques. IEEE Trans. Geosc. and Rem. Sens. Vol. 19(2): 85-90.
80. Smith, J.A., N.S. Chauchan and J. Ballard, 1996. Remote sensing of land surface temperature: the directional viewing effect. . IEEE Trans. Geosci. Rem. Sens. Vol. 13(4): 2146-2148
81. Li, X.-W. and A.H. Strahler, 1985. Geometric-Optical modeling of a conifer forest canopy. IEEE Trans. Geosci. and Rem. Sens. Vol. GE-23 (5): 705-721
82. Su, H.-B, R.-H. Zhang, X..-Z. Tang, X.-M. Sun, Z.-L. Zhu and Z.-L. Li, 2003. An alternative method to compute the component fractions in the geometrical optical model: visual computing method. IEEE Trans. Geosc. and Rem. Sens. Vol. 41(3): 719-724
83. Chen, J.M. and S. Leblanc, 1997. A 4-scale bidirectional reflection model based on canopy architecture. IEEE Trans. Geosc. and Rem. Sens.. Vol. 35:1316-1337.

84. Yu, T., X.-F.Gu, G. -L. Tian, M. Legrand, F Baret, J.-F Hanocq, R. Bosseno and Y. Zhang, 2004. Modeling directional brightness temperature over a maize canopy in row structure. IEEE Trans. Geosc. and Rem. Sens. Vol. 42 (10): 2290 - 2304
85. Gerstl, S.A.W., C.C. Borel and Powers, B.J., 1991. The radiosity method in optical remote sensing of structured 3-D surfaces. Rem. Sens. Env. Vol.36: 13-44
86. Gerstl, S.A.W., Borel, C.C., 1992. Principles of the radiosity method versus radiative transfer for canopy reflectance modelling. IEEE Trans. Geosc. and Rem. Sens. Vol. 30 (2): 271-275
87. Borel, C.C., S.A., Gerstl and B.J. Powers, 1991. The radiosity method in optical remote sensing of structured 3-D surfaces. Remote Sens. Environ. Vol. 36: 13-44
88. Nilson, T., 1971. A theoretical analysis of the frequency of gaps in plant stands. Agric. Meteorol. Vol. 8: 25-38
89. Baret, F., J.P.W. Clevers and M.D. Stevens, 1995. The robustness of canopy gap fraction estimates from the red and near infrared reflectance: a comparison between approaches for sugar beet canopies. Remote Sens. Environ. Vol. 54, 141-151
90. Kimes, D.S. and J.A. Kirchner, 1982. Radiative transfer model for heterogeneous 3-D scenes. Appl Opt, Vol.21 (22):4119-4129
91. Guillevic, P., J.P Gastellu-Etchegorry, J. Demarty and Prévot, L., 2002.Thermal infrared radiative transfer within three-dimensional vegetation. J. Geophys. Res. (Atmospheres), Vol.108(D8): pp. ACL 6-1, ID 4248, DOI 10.1029/2002JD002247
92. Gastellu-Etchegorry, J.P., E. Martin and F. Gascon, 2004. DART: a 3D model for simulating satellite images and studying surface radiation budget. Intern. J. of Rem. Sens. Vol. 25(2):73-96.
93. CESBIO, 2006, DART User Manual v1.1.
94. Welles, J.M. and Norman, J.M., 1991. Photon Transport in discontinuous canopies: a weighted random approach. In: R.B. Myneni and J. Ross, J. (Eds.). Photon-Vegetation Interactions. Applications in Optical Remote Sensing and Plant Ecology. Springer-Verlag, Heidelberg, Germany: 389 – 414
95. Menenti, M., L. Jia, Z.-L. LI, V. Djepa,, J. Wang, M.P. Stoll, Z.B. Su and M. Rast, 2001. Estimation of soil and vegetation temperatures from directional thermal infrared observations: The HEIHE, SGP'97, IMGRASS experiments. J. Geophys. Res.. Vol. 106: 11997 – 2010
96. Jia, L., Z.-L. Li and M. Menenti, 2005. Simulation of Directional Thermal Infrared Radiance Images Using Soil-Vegetation-Atmosphere Heat and Radiation Transfer Models. Proc. 9th Int. Symposium on Physical Measurements and Signatures in Remote Sensing (ISPMSRS) ISSN 1682-1750 ISPRS Vol. XXXVI (7/W20): 331-333
97. Verhoef, W. and H. Bach, 2003. Simulation of hyperspectral and directional radiance images using coupled biophysical and atmospheric radiative transfer models, Rem. Sens. Env. Vol.87: 23-41
98. Norman, J.M. 1979. Modeling the complete crop canopy. In B.J. Barfield and J.F. Gerber (eds.) Modification of the aerial environment of plants. ASAE Monogr. Am. Soc. Agric. Engr., St. Joseph, MI: 249 – 277

99. Norman, J.M. and G.Campbell, 1983. Application of a plant-environment model to problems in irrigation. In: D. Hillel (Ed.) Advanced in irrigation Vol. 2. Academic Press, New York: 155-188
100. Wilson, T.B., J.M. Norman, W.L. Bland, and C.J. Kucharik, 2003. Evaluation of the importance of Lagrangian canopy turbulence formulations in a soil–plant–atmosphere model. Agric. For. Meteorol. Vol. 115: 51–69
101. Verhoef, W and M. Menenti,, 1998. Final Report of Spatial and Spectral Scales of Spaceborne Imaging Spectro-radiometers (SASSSIS). Contract Report 12072/96/NL/CN, ESA. Final Report, NLR-CR-98213, National Aerospace Lab. NLR, Amsterdam, the Netherlands: 314 p
102. Becker, F. and Z.-L. Li, 1995. Surface temperature and emissivity at various scales: definition, measurement and related problems. Remote Sensing Reviews Vol. 12: 225-253.
103. Sobrino, J.A., Z.-L. Li, M.P. Stoll and F. Becker, , 1994. Improvement in the split window technique for land surface temperature determination. IEEE Trans. Geosc. and Rem. Sens. Vol. 32: 243-253
104. Becker, F. and Z. –L Li, 1990. Towards a local split window method over land surfaces. Int. J. Remote Sens. Vol. 11(3):369-393.
105. Frouin, R., P.-Y Deschamps, and P.Lecomte,1990. Determination from space of atmospheric total water vapor amounts by differential absorption near 940nm: Theory and airborne verification. J. Appl. Meteorol. Vol. 29: 448-460
106. Kaufman, Y.J., and Gao, B.-C., 1992,.Remote sensing of water vapor in the near IR from EOS/MODIS. IEEE Trans. Geosc. and Rem. Sens. Vol. 30(5): 871-884.
107. Prabhakara, C., Chang, H.D., and Chang, A.T.C., 1985. Remote sensing of precipitable water over the oceans from NIMBUS 7 microwave measurements. J. Appl. Meteorol. Vol. 21: 59-68
108. Alishouse, J.C., S.A.Snyder, J. Vongsathorn, and R.R Ferraro,., 1990. Determination of oceanic total precipitable water from the SSM/I. IEEE Trans. Geosc. and Rem. Sens. Vol. 28, 811-816
109. Schulz, J., P. Schluessel, , and H. Grassl,, 1993. Water vapor in the atmospheric boundary layer over oceans from SSM/I measurements. Intern. J. of Rem. Sens. Vol. 14: 2773-2789
110. Chesters, D., Uccellini, L.W., and Robinson, P., 1983. Low-level water vapor fields from the VISSR atmospheric sounder (VAS) split-window channels. J. Appl. Meteorol. Vol. 22: 725-743
111. Susskind, J., J. Rosenfield, D. Renter et al., 1984. Remote sensing of weather and climate parameters from HIRS2/MSU on TIROS-N. J. Geophys. Res. Vol. 89: 4677-4697
112. Kleespies, T.J., and McMillin, L.M., 1990. Retrieval of precipitable water from observations in the split window over varying surface temperature. J. Applied Meteorol. Vol. 29: 851-862
113. Jedlovec, G.J., 1990. Precipitable water estimation from high-resolution split window radiance measurements. J. Appl. Meteorol. Vol. 29 : 863-876

114. Iwasaki, H., 1994. Estimation of precipitable water over land using the split-window data from the NOAA satellite. J. Meteorol. Society Japan Vol. 72(2), 223-233.
115. Ottlé, C., Outalha, S., Francois, C., and Le Maguer, S., 1997. Estimation of total atmospheric water vapor content from split-window radiance measurements. R em. Sens. of Env. Vol.61: 410-418
116. Sobrino, J.A., Raissouni, N., Simarro, J., Nerry, F., and Petitcolin, F., 1999, Atmospheric water vapor content over land surfaces derived from AVHRR data: Application to the Iberian Peninsula. IEEE Trans. Geosc. and Rem. Sens. Vol. 37(3): 1425-1434
117. Vermote, E.F., D.Tanre, J.L. Deuze, M.Herman and J.J. Morcrette., 1997. Second simulation of the satellite signal in the solar spectrum, 6S: An overview. IEEE Trans. Geosc. and Rem. Sens. Vol. 35: 675-686
118. Beck, A., Anderson, G.P., Acharya, P.K. et al.,1999. MODTRAN4 User's Manual, Air Force Research Laboratory, Hanscom AFB, MA.
119. Rahman, H., and Dedieu, G.,1994. SMAC: a simplified method for the atmospheric correction of satellite measurements in the solar spectrum. Int. J. of Rem. Sens. Vol.15: 123-143
120. Hapke, B., 1981. Bidirectional reflectance spectroscopy. 1. Theory, J. Geophys. Res. Vol. 86: 3039-3054
121. Flowerdew, R.J. and Haigh, J.D., 1997. Retrieving land surface reflectances using the ATSR-2: A theoretical study. J. Geophys. Res., 102(D14): 17163-17171
122. Mackay, G. and Steven, M.D., 1998. An atmospheric correction procedure for the ATSR-2 visible and near infrared land surface data. Int. J. Remote Sens. Vol.19(15): 2949-2968
123. North, P.R.J., S.A.Briggs, S.E.Plummer, and J.J. Settle, 1999. Retrieval of land surface bi-directional reflectance and aerosol opacity from ATSR-2 multiangle imagery. IEEE Trans. Geosc. and Rem. Sens. Vol. 37(1): 526-537
124. Weiss, M., F. Baret, R. Myneni, A. Pragnère and Y. Knyazikhin, 1999. Investigation of a model inversion technique for the estimation of crop charcteristics from spectral and directional reflectance data. Agronomie Vol. 20: 3-22
125. Verhoef, W., 1998. Theory of radiative transfer models applied in optical remote sensing of vegeation canopies. PhD Thesis, Wageningen University: 311 pp
126. Jia, L., Menenti, M., Su, Z.B., Djepa, V., Li, Z.-L. and Wang, J., 2000. Modeling sensible heat flux using estimates of soil and vegetation temperatures: the HEIFE and IMGRASS experiments." in M. Beniston and M. Verstraete (Eds.) "Satellite remote sensing and climate simulations. " Kluwer, Dordrecht, The Netherlands
127. Hurk, B.J.J.M. van den, L.Jia, C.Jacobs, M.Menenti and Z.-L.Li, 2002. Assimilation of land surface temperature data from ATSR in an NWP environment – a case study. Intern. J. of Rem. Sens. Vol.23(24): 5193-5210
128. Menenti, M., M. Rast, F. Baret, B.v.d. Hurk, W. Knorr,W. Mauser, J. Miller, J. Moreno, M. Schaepman and M. Verstraete, 2005. Understanding vegetation response to climate variability from space: recent advances towards the SPECTRA

Mission. Riv. Ital. Teleril. Special Issue Hyperspectral Observation of Terrestrial Environments. Vol. 33/34: 193 - 206

129. Galeazzi, C., M. Gamache, A. Hollinger, V. De Cosmo, M. Menenti, K. Staenz, J. Beck, M. Bergeron, C. Ananasso, R. Loizzo and M. Maszkiewicz, 2006. ASI-CSA Joint Development Phase for a Hyperspectral Mission. Proc. IMAGING SPECTROSCOPY: Innovation in Environmental Research, Oud Sint-Jan, Bruges, Belgium: (in press)